arXiv:quant-ph/0112140v1 21 Dec 2001

Entangled-Photon Generation from Parametric Down-Conversion in Media with Inhomogeneous Nonlinearity

Giovanni Di Giuseppe,[1*] Mete Atatüre,[2] Matthew D. Shaw,[1] Alexander V. Sergienko,[1,2]
Bahaa E. A. Saleh,[1] and Malvin C. Teich[1,2]

Quantum Imaging Laboratory,[†]

[1]*Department of Electrical & Computer Engineering and* [2]*Department of Physics ,*

Boston University, 8 Saint Mary's Street, Boston, MA 02215

(February 9, 2008)

Abstract

We develop and experimentally verify a theory of Type-II spontaneous parametric down-conversion (SPDC) in media with inhomogeneous distributions of second-order nonlinearity. As a special case, we explore interference effects from SPDC generated in a cascade of two bulk crystals separated by an air gap. The polarization quantum-interference pattern is found to vary strongly with the spacing between the two crystals. This is found to be a cooperative effect due to two mechanisms: the chromatic dispersion of the medium separating the crystals and spatiotemporal effects which arise from the inclusion of transverse wave vectors. These effects provide two concomitant avenues for controlling the quantum state generated in SPDC. We expect

*Also with Istituto Elettrotecnico Nazionale *G. Ferraris*, Strada delle Cacce 91, I-10153 Torino, Italy.

†http://www.bu.edu/qil

these results to be of interest for the development of quantum technologies and the generation of SPDC in periodically varying nonlinear materials.

PACS number(s): 42.50.Dv, 03.65.Bz, 42.65.Ky

Typeset using REVTEX

Contents

I Introduction **4**

II Theory **5**

A State Generation in Inhomogeneous Media 5

1 Periodic Nonlinearity 7

2 Cascaded Bulk Crystals Separated by Linear Media 8

B Two-Photon Amplitude and Fourth-Order Correlation 9

C Quantum Interference with a Cascaded Pair of Bulk Crystals 12

1 Coincidence Detection 13

2 Cascade of Two Identical Crystals 16

3 Small-Aperture Approximation 17

4 Multi-Parameter Formalism: Spatial Effects 20

III Experiment **22**

A Experimental Arrangement 22

B Experimental Results 23

1 Parallel and Antiparallel Optical Axes 23

2 Spatiotemporal Effects 25

IV Conclusion **26**

APPENDIXES **27**

A The Visibility Function $V(\tau)$ **27**

1 Parallel Optical Axes 32

2 Antiparallel Optical Axes 32

B The Function $\mathcal{N}$ **33**

1 Small-Aperture Approximation 34

2 Gaussian-Aperture Approximation 34

I. INTRODUCTION

Spontaneous parametric down-conversion (SPDC) [1] has now come into widespread use as a simple and robust source of entangled photon pairs. Uses for these pairs range from the examination of quantum mechanical foundations [2–4], to applications in optical measurements [5], spectroscopy [6], imaging [7], and quantum information [8,9]. As such, there has been considerable interest in greater optimization and control of the exotic two-photon states available from SPDC, particularly when pumped by ultrafast pulses [10–12]. Additionally, much work has recently been focused on the use of cascaded nonlinear crystals [13–18] to manipulate and improve the generation of the two-photon state.

The photon pairs from Type-II SPDC are generated in a quantum state which can be entangled in frequency, wave vector, and polarization. In recent works [12], we have demonstrated the utility of a model which considers entanglement in these parameters concurrently. It was shown that quantum-interference patterns were altered predictably by controlling the range of transverse wave vectors selected by the optical system. In this paper, we extend this formalism and investigate interference from SPDC generated in media with inhomogeneous longitudinal distributions of nonlinearity. The state function of the photon pair generated in SPDC is completely characterized by three functions: the spectral profile of the pump, the longitudinal distribution of nonlinear susceptibility, and the dispersion in the generation medium. In principle, one could arbitrarily weight the spatiotemporal distribution of signal and idler modes by a judicious choice of these three functions. This, in return, introduces new avenues of control. To demonstrate this, we consider a rudimentary case of an inhomogeneous medium, two bulk crystals separated by a linear medium such as an air gap. In this configuration, a host of interesting effects emerge, such as the modulation of interference visibility with crystal separation. This effect and others are theoretically predicted and experimentally verified in this paper.

The promise of a source whose degree of entanglement is controllable in frequencies and wave vectors by turning a single knob is clearly alluring for purposes of quantum-information processing. The results reported in this paper are also likely to be of use in guiding future developments in quantum-state synthesis involving multi-crystal configurations [13–19], in ultrafast-pumped parametric down-conversion [10,11], and periodically poled materials [20,21].

II. THEORY

Our theory considers a quantum state which can be concurrently entangled in polarization, frequency, and transverse wave vector, so as to be valid for an arbitrary optical system. As we shall see, the longitudinal distribution of nonlinearity provides a powerful means for controlling the structure of the two-photon quantum state generated in SPDC. As an important special case, we consider the simple example of SPDC generation in a cascade of two bulk crystals separated by a linear medium. We then describe the quantum interference between the two photons of the SPDC pair as they propagate through an arbitrary linear optical system. This formalism allows the quantum interference to be analyzed in the absence of spectral filters and reduces to the conventionally established single-mode theory in the small-aperture limit, unless very thick crystals are used.

A. State Generation in Inhomogeneous Media

For the sake of simplicity, we consider media where effects from third- and higher-order susceptibilities are weak and can be neglected. By virtue of the relatively weak interaction in the nonlinear crystal, we consider the two-photon state generated within the confines of first-order time-dependent perturbation theory. The two-photon state at the output of the nonlinear medium is found in the interaction picture to be [12]

$$|\Psi^{(2)}\rangle \propto \int d\mathbf{q}_{\rm o} d\mathbf{q}_{\rm e}\, d\omega_{\rm o} d\omega_{\rm e}\ \Phi(\mathbf{q}_{\rm o}, \mathbf{q}_{\rm e}; \omega_{\rm o}, \omega_{\rm e})\ \hat{a}_{\rm o}^{\dagger}(\mathbf{q}_{\rm o}, \omega_{\rm o})\ \hat{a}_{\rm e}^{\dagger}(\mathbf{q}_{\rm e}, \omega_{\rm e})\ |0\rangle\,, \tag{1}$$

where the state function

$$\Phi(\mathbf{q}_{\rm o},\mathbf{q}_{\rm e};\omega_{\rm o},\omega_{\rm e}) \;=\; \tilde{E}_{\rm p}(\mathbf{q}_{\rm o}+\mathbf{q}_{\rm e};\omega_{\rm o}+\omega_{\rm e}) \int dz\; \chi^{(2)}(z)\; e^{i\Delta(\mathbf{q}_{\rm o},\mathbf{q}_{\rm e};\omega_{\rm o},\omega_{\rm e})z}\,. \tag{2}$$

Here $\chi^{(2)}(z)$ is the distribution of second-order nonlinearity along the longitudinal axis, $\tilde{E}_{\rm p}(\mathbf{q}_{\rm p};\omega_{\rm p})$ is the complex-amplitude profile of the pump field, $\mathbf{q}_j$ ($j={\rm p,o,e}$) is the transverse component of the wave vector $\mathbf{k}_j$ in the medium, and Δ is the wave vector mismatch function

$$\Delta(\mathbf{q}_{\rm o},\mathbf{q}_{\rm e};\omega_{\rm o},\omega_{\rm e}) = \kappa_{\rm p}(\omega_{\rm o}+\omega_{\rm e},\mathbf{q}_{\rm o}+\mathbf{q}_{\rm e}) - \kappa_{\rm o}\left(\omega_{\rm o},\mathbf{q}_{\rm o}\right) - \kappa_{\rm e}\left(\omega_{\rm e},\mathbf{q}_{\rm e}\right), \tag{3}$$

which depends on the dispersiveness of the medium. In this equation, the longitudinal projections κ_j ($j={\rm p,o,e}$) are related to the indices $(\mathbf{q}_j,\omega_j)$ via

$$\kappa_j(\omega_j,\mathbf{q}_j) = \sqrt{k_j^2(\omega_j,\mathbf{q}_j) - |\mathbf{q}_j|^2}, \tag{4}$$

where $\omega_{\rm p}=\omega_{\rm o}+\omega_{\rm e}$ and $\mathbf{q}_{\rm p}=\mathbf{q}_{\rm o}+\mathbf{q}_{\rm e}$. Here the wavenumber $k_j \equiv |\mathbf{k}_j| = n[\omega_j,\theta(\mathbf{q}_j)]\,\omega_j/c$, where c is the speed of light in vacuum, θ is the angle between $\mathbf{k}_{\rm p}$ and the optical axis of the nonlinear crystal, and $n(\omega_j,\theta)$ is the index of refraction in the nonlinear medium. Note that the symbol $n(\omega,\theta)$ represents the extraordinary refractive index $n_{\rm e}(\omega,\theta)$ when calculating κ for extraordinary waves, and the ordinary refractive index $n_{\rm o}(\omega)$ for ordinary waves.

Note from Eq. (2) that the state function is completely characterized by the spectral profile of the pump, the longitudinal distribution of nonlinear susceptibility, and the dispersion in the generation medium. All three of these parameters may be controlled experimentally, and all three present avenues for controlling the structure of the two-photon quantum state.

For a medium with an inhomogeneous distribution of nonlinear susceptibility along the longitudinal axis, it is convenient to define

$$\chi^{(2)}(z) = \int d\zeta\, \tilde{\chi}^{(2)}(\zeta)\, e^{-i\zeta z}\,, \tag{5}$$

where $\tilde{\chi}^{(2)}(\zeta)$ is the inverse Fourier transform of $\chi^{(2)}(z)$. Substitution into Eq. (2) then gives

$$\Phi(\mathbf{q}_{\rm o},\mathbf{q}_{\rm e};\omega_{\rm o},\omega_{\rm e}) \;=\; \tilde{E}_{\rm p}(\mathbf{q}_{\rm o}+\mathbf{q}_{\rm e};\omega_{\rm o}+\omega_{\rm e})\; \tilde{\chi}^{(2)}[\Delta(\mathbf{q}_{\rm o},\mathbf{q}_{\rm e};\omega_{\rm o},\omega_{\rm e})] \tag{6}$$

for a uniformly dispersive medium. For example, a single bulk crystal of thickness L and constant nonlinearity χ_0 has a nonlinear susceptibility profile $\chi^{(2)}(z) = \chi_0 \mathrm{rect}_{[-L,0]}(z)$ where $\mathrm{rect}_{[-L,0]}(z) = 1$ if $-L \leq z \leq 0$ and zero otherwise. In this case, the inverse Fourier transform of the nonlinearity profile becomes

$$\tilde{\chi}^{(2)}(\Delta) = \chi_0 L \ \mathrm{sinc}\left(\frac{L\Delta}{2}\right) e^{-\mathrm{i}\frac{L\Delta}{2}} \,. \tag{7}$$

For a monochromatic plane wave pump with a central frequency ω_p^0, $\tilde{E}_\mathrm{p}(\mathbf{q}_\mathrm{p};\omega_\mathrm{p})$ in Eq. (6) is proportional to $\delta(\mathbf{q}_\mathrm{o} + \mathbf{q}_\mathrm{e})\delta(\omega_\mathrm{o} + \omega_\mathrm{e} - \omega_\mathrm{p}^0)$ and the state function Φ for SPDC reduces to $\tilde{\chi}^{(2)}\left[\Delta(\mathbf{q}, -\mathbf{q}; \omega, \omega_\mathrm{p}^0 - \omega)\right]$. Figure 1(a) shows the absolute square of the state function in Eq. (7), the familiar $\mathrm{sinc}^2(L\Delta/2)$ distribution of SPDC from a single bulk crystal.

1. Periodic Nonlinearity

We now consider a medium of thickness L with a periodic distribution of nonlinear susceptibility $\chi^{(2)}(z) = \chi^{(2)}(z + \Lambda)$ within the medium. Such materials are widely used in classical nonlinear optics [20] and have recently been employed for generation of SPDC [21]. We may write

$$\chi^{(2)}(z) = \chi_0 g(z) \, \mathrm{rect}_{[-L,0]}(z) \,, \tag{8}$$

where $g(z)$ can be expressed in the Fourier series

$$g(z) = \sum_{m=-\infty}^{\infty} G_m \ e^{\mathrm{i}K_m z} \tag{9}$$

with $K_m \equiv 2\pi m/\Lambda$. The Fourier Transform of Eq. (8) is then given by

$$\tilde{\chi}^{(2)}(\Delta) = \chi_0 L \sum_{m=-\infty}^{\infty} G_m \ \mathrm{sinc}\left[\frac{L}{2}(\Delta + K_m)\right] e^{-\mathrm{i}\frac{L}{2}(\Delta + K_m)} \,. \tag{10}$$

For example, let us consider the case of a sinusoidal distribution of nonlinear susceptibility with period Λ, for which

$$\chi^{(2)}(z) = \chi_0 \cos\left(\frac{2\pi}{\Lambda} z\right) \mathrm{rect}_{[-L,0]}(z) \,, \tag{11}$$

which yields

$$\tilde{\chi}^{(2)}(\Delta) \;=\; \chi_0 L \left\{ \mathrm{sinc}\left[\frac{L}{2}\left(\Delta + \frac{2\pi}{\Lambda}\right)\right] e^{-\mathrm{i}\frac{L}{2}\left(\Delta+\frac{2\pi}{\Lambda}\right)} + \mathrm{sinc}\left[\frac{L}{2}\left(\Delta - \frac{2\pi}{\Lambda}\right)\right] e^{-\mathrm{i}\frac{L}{2}\left(\Delta-\frac{2\pi}{\Lambda}\right)} \right\} . \quad (12)$$

In this case, we obtain phase-matching conditions similar to the first-order quasi-phase matching (QPM) observed in periodically poled nonlinear crystals. The extra component $\pm 2\pi/\Lambda$ above is analogous to the grating vector in first-order QPM. Figure 1(b) shows the absolute square of the state function of the down-converted light obtained from a single crystal with the nonlinearity profile given in Eq. (11).

2. Cascaded Bulk Crystals Separated by Linear Media

A simple example of a medium with an inhomogeneous distribution of nonlinearity is a cascade of multiple bulk crystals separated by linear dielectrics. Consider, for example, a cascade of N bulk crystals separated by $N-1$ linear media. Let each nonlinear crystal j have thickness L_j, constant nonlinearity χ_{0_j}, and separation distance d_j from the previous crystal. The overall nonlinear susceptibility of this system is then given by

$$\chi^{(2)}(z) = \sum_{j=1}^{N} \epsilon_j \chi_{0_j}\, \mathrm{rect}_{[-L_j,0]}\left[z + \sum_{k=j+1}^{N} (d_k + L_k)\right] , \quad (13)$$

where the terms of the summation inside the rect function are taken to be zero if $k > N$. Here $\epsilon = \pm 1$ represents the sign of the quadratic susceptibility, which depends on the orientation of the optical axis of the j-th crystal. Note that in this equation, the $z = 0$ point is placed at the output plane of the last crystal. In such a configuration, the function $\tilde{\chi}^{(2)}(\Delta)$ in Eq. (6) becomes

$$\tilde{\chi}^{(2)}(\Delta) \;=\; \sum_{j=1}^{N} \epsilon_j \chi_{0_j}\, L_j\, \mathrm{sinc}\left(\frac{L_j \Delta_j}{2}\right) e^{-\mathrm{i}\frac{L_j\Delta_j}{2}}\, e^{-\mathrm{i}\sum_{k=j+1}^{N}\left(L_k\Delta_k + d_k\Delta'_k\right)} \quad (14)$$

where the wave vector mismatch function Δ_j is independent of z and Δ'. As seen from Eq. (3), Δ' depends on the dispersiveness of the linear medium [14].

We now consider the particular case of a cascade of two bulk crystals of the same material [See Fig. 2(a)] separated by a linear but dispersive medium. The explicit form of the nonlinearity is given by

$$\chi^{(2)}(z) = \chi_0 \,\mathrm{rect}_{[-L_1,0]}(z+d+L_2) + \epsilon\,\chi_0\,\mathrm{rect}_{[-L_2,0]}(z)\,, \tag{15}$$

where $\epsilon = +1$ if the optical axes of the two crystals are parallel and $\epsilon = -1$ if the optical axes are antiparallel. For such a configuration

$$\tilde{\chi}^{(2)}(\Delta) \;=\; \chi_0 \left\{ L_1 \,\mathrm{sinc}\left(\frac{L_1\Delta}{2}\right) e^{-\mathrm{i}\frac{L_1\Delta}{2}}\, e^{\mathrm{i}(L_2\Delta + d\Delta')} + \epsilon\, L_2 \,\mathrm{sinc}\left(\frac{L_2\Delta}{2}\right) e^{-\mathrm{i}\frac{L_2\Delta}{2}} \right\}. \tag{16}$$

The absolute square of the state function of SPDC in this configuration is given in Fig. 2(a), where the envelope is governed solely by the dispersion in the nonlinear crystals. The period of the modulation inside this envelope is determined primarily by the dispersion in the linear medium between the crystals, while the amplitude of this modulation is determined by the ratio of the crystal thicknesses. Figure 2(b) shows the absolute square of the state function in the special case of two bulk crystals of the same material with the same thickness. In this condition the amplitude of the modulation inside the envelope is maximized.

B. Two-Photon Amplitude and Fourth-Order Correlation

We now consider the propagation of the down-converted light through an arbitrary linear optical system to a pair of detectors, as illustrated in Fig. 3. The joint probability amplitude of detecting the photon pair at the space-time coordinates $(\mathbf{x}_\mathrm{A}, t_\mathrm{A})$ and $(\mathbf{x}_\mathrm{B}, t_\mathrm{B})$ is given by

$$A(\mathbf{x}_\mathrm{A}, t_\mathrm{A}; \mathbf{x}_\mathrm{B}, t_\mathrm{B}) = \langle 0|\hat{E}^{(+)}_\mathrm{A}(\mathbf{x}_\mathrm{A}, t_\mathrm{A})\hat{E}^{(+)}_\mathrm{B}(\mathbf{x}_\mathrm{B}, t_\mathrm{B})|\Psi^{(2)}\rangle \tag{17}$$

where $E^{(+)}_\mathrm{A}$ and $E^{(+)}_\mathrm{B}$ are the positive-frequency components of the electric fields at points A and B. The explicit forms of the quantum fields present at the detection locations are given by

$$\begin{aligned}
\hat{E}^{(+)}_\mathrm{A}(\mathbf{x}_\mathrm{A}, t_\mathrm{A}) &= \sum_{j=\mathrm{e,o}} \int d\mathbf{q}\, d\omega\; e^{-\mathrm{i}\omega t_\mathrm{A}}\; \mathcal{H}_{\mathrm{A}j}(\mathbf{x}_\mathrm{A}, \mathbf{q}; \omega)\; \hat{a}_j(\mathbf{q}, \omega)\,, \\
\hat{E}^{(+)}_\mathrm{B}(\mathbf{x}_\mathrm{B}, t_\mathrm{B}) &= \sum_{j=\mathrm{e,o}} \int d\mathbf{q}\, d\omega\; e^{-\mathrm{i}\omega t_\mathrm{B}}\; \mathcal{H}_{\mathrm{B}j}(\mathbf{x}_\mathrm{B}, \mathbf{q}; \omega)\; \hat{a}_j(\mathbf{q}, \omega)\,,
\end{aligned} \tag{18}$$

where the transfer function $\mathcal{H}_{ij}$ ($i = \mathrm{A,B}$ and $j = \mathrm{e,o}$) describes the propagation of a mode $(\mathbf{q}, \omega)$ through the optical system from the output plane of the nonlinear medium to the

detection plane. Substitution of Eqs. (1) and (18) into Eq. (17) yields a general form for the two-photon detection probability amplitude,

$$A(\mathbf{x}_{\rm A}, t_{\rm A}; \mathbf{x}_{\rm B}, t_{\rm B}) = A_{\rm Ao,Be}(\mathbf{x}_{\rm A}, t_{\rm A}; \mathbf{x}_{\rm B}, t_{\rm B}) + A_{\rm Bo,Ae}(\mathbf{x}_{\rm A}, t_{\rm A}; \mathbf{x}_{\rm B}, t_{\rm B}) \tag{19}$$

where the probability amplitude $A_{\rm Ao,Be}$ for finding the signal photon in arm A and the idler photon in arm B is defined as

$$A_{\rm Ao,Be}(\mathbf{x}_{\rm A}, t_{\rm A}; \mathbf{x}_{\rm B}, t_{\rm B}) = \int d\mathbf{q}_{\rm o} d\mathbf{q}_{\rm e}\, d\omega_{\rm o} d\omega_{\rm e}\ \Phi(\mathbf{q}_{\rm o}, \mathbf{q}_{\rm e}; \omega_{\rm o}, \omega_{\rm e})\ e^{-{\rm i}(\omega_{\rm o} t_{\rm A} + \omega_{\rm e} t_{\rm B})} \times \mathcal{H}_{\rm Ao}(\mathbf{x}_{\rm A}, \mathbf{q}_{\rm o}; \omega_{\rm o})\ \mathcal{H}_{\rm Be}(\mathbf{x}_{\rm A}, \mathbf{q}_{\rm e}; \omega_{\rm e}) \tag{20}$$

and $A_{\rm Bo,Ae}(\mathbf{x}_{\rm A}, t_{\rm A}; \mathbf{x}_{\rm B}, t_{\rm B})$ is obtained by exchanging the indices A $\leftrightarrow$ B.

The joint probability density for detection of the signal and idler photons at space-time points $(\mathbf{x}_{\rm A}, t_{\rm A})$ and $(\mathbf{x}_{\rm B}, t_{\rm B})$ is given by the fourth-order correlation function, is given by the absolute square of Eq. (19):

$$G^{(2)}(\mathbf{x}_{\rm A}, t_{\rm A}; \mathbf{x}_{\rm B}, t_{\rm B}) = |A_{\rm Ao,Be}(\mathbf{x}_{\rm A}, t_{\rm A}; \mathbf{x}_{\rm B}, t_{\rm B})|^2 + |A_{\rm Bo,Ae}(\mathbf{x}_{\rm A}, t_{\rm A}; \mathbf{x}_{\rm B}, t_{\rm B})|^2 + 2\,\Re e[A^*_{\rm Ao,Be}(\mathbf{x}_{\rm A}, t_{\rm A}; \mathbf{x}_{\rm B}, t_{\rm B})\ A_{\rm Bo,Ae}(\mathbf{x}_{\rm A}, t_{\rm A}; \mathbf{x}_{\rm B}, t_{\rm B})]. \tag{21}$$

With current technology, quantum interferometry is performed using slow detectors that cannot resolve signals on the characteristic time scale of down-conversion (the inverse of down-conversion bandwidth), which is typically less than 1 ps. In addition, the detectors used in our experiments have a large active area compared to the width of the SPDC beams at the detection planes. Under these conditions, the coincidence count rate R is readily expressed in terms of the two-photon detection probability amplitude A by integrating the fourth-order correlation function $G^{(2)}(\mathbf{x}_{\rm A}, t_{\rm A}; \mathbf{x}_{\rm B}, t_{\rm B})$ over all space and time,

$$R = \int dt_{\rm A} dt_{\rm B}\, d\mathbf{x}_{\rm A} d\mathbf{x}_{\rm B}\ |A(\mathbf{x}_{\rm A}, t_{\rm A}; \mathbf{x}_{\rm B}, t_{\rm B})|^2 . \tag{22}$$

This expression for the count rate can be separated into two terms as

$$R = R_0 + R_{\rm int}\,, \tag{23}$$

where the baseline term is

$$R_0 = \int d\omega' d\omega \, d\mathbf{q}_{\rm o} d\mathbf{q}_{\rm e} \, d\mathbf{q}'_{\rm o} d\mathbf{q}'_{\rm e} \; \Phi(\mathbf{q}_{\rm o}, \mathbf{q}_{\rm e}; \omega, \omega') \; \Phi^*(\mathbf{q}'_{\rm o}, \mathbf{q}'_{\rm e}; \omega, \omega') \times \left[\mathcal{S}_{\rm AB}(\mathbf{q}_{\rm o}, \mathbf{q}_{\rm e}, \mathbf{q}'_{\rm o}, \mathbf{q}'_{\rm e}; \omega, \omega') + \mathcal{S}_{\rm BA}(\mathbf{q}_{\rm o}, \mathbf{q}_{\rm e}, \mathbf{q}'_{\rm o}, \mathbf{q}'_{\rm e}; \omega, \omega')\right] \quad (24)$$

and the interference term is

$$R_{\rm int} = 2\Re e \int d\omega' d\omega \, d\mathbf{q}_{\rm o} \; d\mathbf{q}_{\rm e} \, d\mathbf{q}'_{\rm o} d\mathbf{q}'_{\rm e} \; \Phi(\mathbf{q}_{\rm o}, \mathbf{q}_{\rm e}; \omega', \omega) \; \Phi^*(\mathbf{q}'_{\rm o}, \mathbf{q}'_{\rm e}; \omega, \omega') \; \mathcal{S}_{\rm AB}(\mathbf{q}_{\rm e}, \mathbf{q}_{\rm o}, \mathbf{q}'_{\rm o}, \mathbf{q}'_{\rm e}; \omega, \omega') \, . \quad (25)$$

In Eqs. (24) and (25) the state function Φ weights the signal and idler modes in the process of generation, while the function $\mathcal{S}_{AB}$ weights these modes in the process of propagation through the optical system. Explicitly,

$$\mathcal{S}_{\rm AB}(\mathbf{q}_{\rm e}, \mathbf{q}_{\rm o}, \mathbf{q}'_{\rm o}, \mathbf{q}'_{\rm e}; \omega, \omega') = \langle \mathcal{H}^*_{\rm Ao}(\mathbf{x}_{\rm A}, \mathbf{q}'_{\rm o}; \omega) \; \mathcal{H}_{\rm Ao}(\mathbf{x}_{\rm A}, \mathbf{q}_{\rm o}; \omega) \rangle_{\mathbf{x}_{\rm A}} \; \langle \mathcal{H}^*_{\rm Be}(\mathbf{x}_{\rm B}, \mathbf{q}'_{\rm e}; \omega') \; \mathcal{H}_{\rm Be}(\mathbf{x}_{\rm B}, \mathbf{q}_{\rm e}; \omega') \rangle_{\mathbf{x}_{\rm B}} \quad (26)$$

where $\langle \cdot \rangle_{\mathbf{x}_i}$ indicates integration over the total detector area.

Note from Eqs. (19) and (20) that the two-photon detection probability amplitude is completely specified by $\mathcal{H}_{ij}$ ($i = \mathrm{A}, \mathrm{B}$ and $j = \mathrm{o}, \mathrm{e}$), $\Phi(\mathbf{q}_{\rm o}, \mathbf{q}_{\rm e}; \omega_{\rm o}, \omega_{\rm e})$, and the physical location of detectors A and B. As we have seen in Eq. (6), we may control the structure of the state function Φ by a judicious choice of the pump spectral profile, the longitudinal distribution of nonlinearity, and the dispersion in the crystal. We may further control the two-photon detection amplitude, and hence the quantum-interference pattern, through the choice of the optical system. Note that states with different state functions can lead to the same quantum-interference pattern through an appropriate design of the optical system.

In the experimentally relevant case of a monochromatic plane wave pump field, Eqs. (24) and (25) become

$$R_0 = \int d\omega \int d\mathbf{q} \; d\mathbf{q}' \; \tilde{\chi}^{(2)*}[\Delta(\mathbf{q}', -\mathbf{q}'; \omega, \omega_{\rm p}^0 - \omega)] \; \tilde{\chi}^{(2)}[\Delta(\mathbf{q}, -\mathbf{q}; \omega, \omega_{\rm p}^0 - \omega)] \times \left[\bar{\mathcal{S}}_{\rm AB}(\mathbf{q}, \mathbf{q}'; \omega) + \bar{\mathcal{S}}_{\rm BA}(\mathbf{q}, \mathbf{q}'; \omega)\right] \quad (27)$$

and

$$R_{\rm int} = 2\Re e \int d\mathbf{q}\; d\mathbf{q}'\; \tilde{\chi}^{(2)*}[\Delta(\mathbf{q}', -\mathbf{q}'; \omega_{\rm p}^0 - \omega, \omega)]\; \tilde{\chi}^{(2)}[\Delta(\mathbf{q}, -\mathbf{q}; \omega, \omega_{\rm p}^0 - \omega)]\; \bar{\mathcal{S}}_{\rm AB}(\mathbf{q}, -\mathbf{q}'; \omega) \quad (28)$$

where we use the shorthand

$$\bar{\mathcal{S}}_{\rm AB}(\mathbf{q}, \mathbf{q}'; \omega) = \mathcal{S}_{\rm AB}(\mathbf{q}, -\mathbf{q}, \mathbf{q}', -\mathbf{q}'; \omega, \omega_{\rm p}^0 - \omega). \quad (29)$$

Thus we see that for a monochromatic plane wave pump, the quantum-interference pattern is critically dependent on the form of $\tilde{\chi}^{(2)}(\Delta)$, which we are free to choose as a design parameter [20]. In principle, the only limitation on the class of amplitudes A which we are able to prepare with this method is the restriction that the optical system is linear.

C. Quantum Interference with a Cascaded Pair of Bulk Crystals

We now apply the above formalism to the case of two cascaded bulk crystals separated by a dispersive but linear dielectric medium such as an air gap. For simplicity, we again consider the medium to be pumped by a monochromatic plane wave. Owing to the structure of the nonlinearity for this particular case [Eq. (15)], the overall two-photon detection probability amplitude is the sum of the two amplitudes associated with each single crystal [14,18]. Each of the amplitudes in Eq. (19) can then be written as

$$A_{\rm Ao,Be}(\mathbf{x}_{\rm A}, t_{\rm A}; \mathbf{x}_{\rm B}, t_{\rm B}) = A^{(1)}_{\rm Ao,Be}(\mathbf{x}_{\rm A}, t_{\rm A}; \mathbf{x}_{\rm B}, t_{\rm B}) + \epsilon\; A^{(2)}_{\rm Ao,Be}(\mathbf{x}_{\rm A}, t_{\rm A}; \mathbf{x}_{\rm B}, t_{\rm B}) \quad (30)$$

where $\epsilon = \pm 1$ as in Eq. (15), and a similar expression for $A_{\rm Bo,Ae}$ is obtained by exchanging the indices A $\leftrightarrow$ B. $A^{(r)}_{\rm Ao,Be}$ for $r = (1, 2)$ is the probability amplitude of finding the o-polarized photon generated in the r-th crystal in arm A and the e-polarized photon from the r-th crystal in arm B. From Eq. (20),

$$A^{(r)}_{\rm Ao,Be}(\mathbf{x}_{\rm A}, \mathbf{x}_{\rm B}; t) = \int d\nu\, d\mathbf{q}\, e^{-i\nu t} \tilde{\chi}^{(2)}_r(\mathbf{q}, \nu)\; \mathcal{H}_{\rm Ao}(\mathbf{x}_{\rm A}; \mathbf{q}, \nu)\; \mathcal{H}_{\rm Be}(\mathbf{x}_{\rm B}; -\mathbf{q}, -\nu) \quad (31)$$

where the angular frequency $\nu = \omega - \omega_{\rm p}^0/2$ is the deviation from the central frequency $\omega_{\rm p}^0/2$, $t = t_{\rm A} - t_{\rm B}$ is the time difference between detection events, and $\tilde{\chi}^{(2)}_r(\mathbf{q}, \nu)$ is the inverse Fourier transform of the nonlinearity profile of the r-th crystal. $A^{(r)}_{\rm Bo,Ae}$ is likewise obtained

by a suitable exchange of the indices. Note that we have omitted an overall phase factor $\exp[-i\omega_{\rm p}^0(t_{\rm A}+t_{\rm B})/2]$ which appears outside the integral in Eq. (31), since in experimental practice we are interested only in the absolute square $|A(\mathbf{x}_{\rm A},t_{\rm A};\mathbf{x}_{\rm B},t_{\rm B})|^2$, so this factor does not introduce any relative phase between the terms of Eq. (19).

As we are considering bulk crystals, the nonlinearity profile of each crystal r is uniform, and thus

$$\tilde{\chi}_r^{(2)}(\mathbf{q},\nu)=\chi_0 Q_r\left(\mathbf{q},\nu\right)\cdot\int dz\ \mathrm{rect}_{[-L_r,0]}(z)\ e^{i\Delta_r(\mathbf{q},\nu)z}\,, \tag{32}$$

where

$$Q_r\left(\mathbf{q},\nu\right)=e^{-i[d\Delta'(\mathbf{q},\nu)+L_2\Delta_2(\mathbf{q},\nu)]\ \delta_{r,1}} \tag{33}$$

is the transfer function for propagation of the signal (o-polarized) and idler (e-polarized) fields generated in the first crystal through the linear dispersive medium of thickness d and thence through the second crystal of thickness L_2. Alternatively, $Q_r\left(\mathbf{q},\nu\right)$ may be thought of as the phase accumulated in the shift of the rect function for the first crystal by a distance $-(L_2+d)$. As given in Eq. (3), Δ_r is the wave vector mismatch function due to dispersion in the r-th crystal and Δ' is the wave vector mismatch function due to dispersion in the linear medium. The symbol $\delta_{r,1}$ represents the Kronecker delta where $\delta_{1,1}=1$ and $\delta_{2,1}=0$.

1. Coincidence Detection

Taking the absolute square of Eq. (30) gives interference between the probability amplitudes of finding a pair generated in the first crystal and finding a pair generated in the second crystal. Indeed, substitution of Eqs. (19) and (30) into Eq. (22) gives the coincidence count rate as a sum of three contributions

$$R=R^{(1)}+R^{(2)}+R^{(12)} \tag{34}$$

where the first two terms are the coincidence-count rates for single-crystal SPDC, and the last term arises as interference between the two single-crystal amplitudes. Recalling Eq. (23), each term in Eq. (34) can in turn be broken down into baseline and interference terms

$$R^{(h)} = R_0^{(h)} + R_{\rm int}^{(h)} \tag{35}$$

where $h = 1, 2, 12$.

We now use this theory to predict quantum-interference patterns in the interferometer shown in Fig. 4. In this system, the transfer function $\mathcal{H}_{ij}$ is separable into diffraction-dependent and -independent factors as

$$\mathcal{H}_{ij}(\mathbf{x}_j; \mathbf{q}, \nu) = H_i(\mathbf{x}_i; \mathbf{q}, \nu)\, \mathcal{T}_{ij}\, e^{i\kappa_j(\mathbf{q},\nu) l_\tau} \tag{36}$$

where the polarization-independent components are grouped into H_i and the remainder are grouped into $\mathcal{T}_{ij}\, e^{i\kappa_j(\mathbf{q},\nu) l_\tau}$. In this case, $\mathcal{T}_{ij} = (\mathbf{e}_i \cdot \mathbf{e}_j)$ is the projection of the unit photon polarization vector $\mathbf{e}_j$ ($j = \mathrm{o}, \mathrm{e}$) onto the axis of the polarization analyzer in front of detector $i = (\mathrm{A}, \mathrm{B})$, and the exponential factor is the transfer function of the delay line.

The delay line, which is often treated as a simple phase shift, is a dispersive optical element which may alter the spatial and/or the spectral profile of the two-photon probability amplitude. Experimentally, the delay line consists of a birefringent quartz plate of variable thickness, modelled by the propagation function $e^{i\kappa_j(\mathbf{q},\nu) l_\tau}$, where the longitudinal projections κ_j of the signal and idler wave vectors are defined in Eq. (4) and l_τ is the thickness of the birefringent plate, which induces a relative optical-path delay τ. This propagation function, while here used to describe the delay line, is technically a valid transfer function for any nonabsorbing dispersive optical element.

Given this particular optical system, then, the single-crystal coincidence-count rates are given by

$$\begin{aligned} R_0^{(r)} = \int d\nu\, d\mathbf{q} d\mathbf{q}'\, \mathcal{F}_{\rm AB}(\mathbf{q}, \mathbf{q}', \nu)\; e^{-{\rm i}[\eta_\tau(\mathbf{q},\nu) - \eta_\tau(\mathbf{q}',\nu)]} \\ \times \left[\mu_{\rm Ao,Be}^2\; \tilde{\chi}_r^{(2)*}(\mathbf{q}', \nu)\; \tilde{\chi}_r^{(2)}(\mathbf{q}, \nu) + \mu_{\rm Bo,Ae}^2\; \tilde{\chi}_r^{(2)*}(-\mathbf{q}', -\nu)\; \tilde{\chi}_r^{(2)}(-\mathbf{q}, -\nu)\right] \end{aligned} \tag{37}$$

and

$$\begin{aligned} R_{\rm int}^{(r)} = \int d\nu\, d\mathbf{q} d\mathbf{q}'\, \mathcal{F}_{\rm AB}(\mathbf{q}, -\mathbf{q}', \nu)\; e^{-{\rm i}[\eta_\tau(\mathbf{q},\nu) - \eta_\tau(\mathbf{q}',-\nu)]} \\ \times \mu_{\rm Ao,Be}\; \mu_{\rm Bo,Ae} \left[\tilde{\chi}_r^{(2)*}(\mathbf{q}', -\nu)\; \tilde{\chi}_r^{(2)}(\mathbf{q}, \nu) + \tilde{\chi}_r^{(2)*}(-\mathbf{q}', \nu)\; \tilde{\chi}_r^{(2)}(-\mathbf{q}, -\nu)\right] \end{aligned} \tag{38}$$

where $r = 1, 2$ is the crystal index, $\mu_{ij,lm} = \mathcal{T}_{ij} \cdot \mathcal{T}_{lm}$ ($i, l = \mathrm{A}, \mathrm{B}$ and $j, m = \mathrm{e}, \mathrm{o}$) is the projection of the polarization of the i-th photon onto the j-th basis polarization and the polarization of the l-th photon onto the m-th basis polarization, and the phase function

$$\eta_\tau(\mathbf{q}, \nu) = -\left[\kappa_\mathrm{o}\left(\nu, \mathbf{q}\right) + \kappa_\mathrm{e}\left(-\nu, -\mathbf{q}\right)\right] l_\tau \tag{39}$$

depends on the dispersion introduced by the delay line. The integral over the detection planes

$$\mathcal{F}_\mathrm{AB}(\mathbf{q}, \pm\mathbf{q}', \nu) = \langle H_\mathrm{A}\left(\mathbf{x}_\mathrm{A}, \mathbf{q}; \nu\right)\ H_\mathrm{A}^*\left(\mathbf{x}_\mathrm{A}, \pm\mathbf{q}'; \nu\right)\rangle_{\mathbf{x}_\mathrm{A}} \langle H_\mathrm{B}\left(\mathbf{x}_\mathrm{B}, -\mathbf{q}; -\nu\right)\ H_\mathrm{B}^*\left(\mathbf{x}_\mathrm{B}, \mp\mathbf{q}'; -\nu\right)\rangle_{\mathbf{x}_\mathrm{B}} \tag{40}$$

is an analog of the function $\bar{\mathcal{S}}_\mathrm{AB}$ for the polarization-independent elements of the system only.

Meanwhile, the coincidence-count rates which arise collectively between the contributions from the two crystals are given by

$$\begin{aligned} R_0^{(12)} = \epsilon \int d\nu\, d\mathbf{q} d\mathbf{q}'\, \mathcal{F}_\mathrm{AB}(\mathbf{q}, \mathbf{q}', \nu)\ e^{-\mathrm{i}[\eta_\tau(\mathbf{q},\nu) - \eta_\tau(\mathbf{q}',\nu)]} \\ \times \sum_{r=1,2} \left[\mu^2_\mathrm{Ao,Be}\ \tilde{\chi}_r^{(2)*}(\mathbf{q}', \nu)\ \tilde{\chi}_{3-r}^{(2)}(\mathbf{q}, \nu) + \mu^2_\mathrm{Bo,Ae}\ \tilde{\chi}_r^{(2)*}(-\mathbf{q}', -\nu)\ \tilde{\chi}_{3-r}^{(2)}(-\mathbf{q}, -\nu)\right] \end{aligned} \tag{41}$$

and

$$\begin{aligned} R_\mathrm{int}^{(12)} = \epsilon \int d\nu\, d\mathbf{q} d\mathbf{q}'\, \mathcal{F}_\mathrm{AB}(\mathbf{q}, -\mathbf{q}', \nu)\ e^{-\mathrm{i}[\eta_\tau(\mathbf{q},\nu) - \eta_\tau(\mathbf{q}',-\nu)]} \\ \times \mu_\mathrm{Ao,Be}\ \mu_\mathrm{Bo,Ae} \sum_{r=1,2} \left[\tilde{\chi}_r^{(2)*}(\mathbf{q}', -\nu)\ \tilde{\chi}_{3-r}^{(2)}(\mathbf{q}, \nu) + \tilde{\chi}_r^{(2)*}(-\mathbf{q}', \nu)\ \tilde{\chi}_{3-r}^{(2)}(-\mathbf{q}, -\nu)\right] . \end{aligned} \tag{42}$$

By combining Eqs. (37), (38), (41), and (42), the overall coincidence-count rate $R(\tau)$ can be organized into a general form

$$R(\tau) = R_0\left[1 + v_\mathrm{pol} V(\tau)\right] \tag{43}$$

where R_0 is the baseline coincidence-count rate and the overall projection of both photon polarizations onto the basis of the polarization analyzers is given by the factor

$$v_\mathrm{pol} = 2\frac{\mu_\mathrm{Ao,Be}\ \mu_\mathrm{Bo,Ae}}{\mu^2_\mathrm{Ao,Be} + \mu^2_\mathrm{Bo,Ae}} . \tag{44}$$

Observe that the τ-dependence of the quantum interference pattern is then contained solely in the visibility function $V(\tau)$.

In the experiments presented in this paper, the two crystals are of the same material and have equal thicknesses L. The apertures are symmetric for both transverse directions, and the analyzers are set 45° from the optical axis, so $v_{\rm pol} = -1$. No spectral filters are used. For these conditions, the explicit form of the visibility function in Eq. (43) becomes

$$\begin{aligned} V(\tau) = & \frac{1}{1+\rho^2}\int dz\ \Pi_L(z)\ \Pi_L\left(\frac{2\tau}{D} - 2L - z\right)\ \mathcal{G}^{(1)}\left(\frac{z}{L};\frac{\tau}{LD}\right) \\ & + \frac{1}{1+\rho^2}\int dz\ \Pi_L(z)\ \Pi_L\left(\frac{2\tau}{D} - z\right)\ \mathcal{G}^{(2)}\left(\frac{z}{L};\frac{\tau}{LD}\right) \\ & + 2\epsilon\frac{\rho}{1+\rho^2}\int dz\ \Pi_L(z)\ \Pi_L\left(\frac{2\tau}{D} - L - z\right)\ \Re e\left[\mathcal{G}^{(12)}\left(\frac{z}{L}+\frac{1}{2};\frac{\tau}{LD}\right)\ e^{-i\Delta' d}\right] \end{aligned} \tag{45}$$

where $\mathcal{G}^{(h)}$ is defined in Appendix A, $\rho = (d_1 + d)/d_1$, $\Pi_L(z)$ is the unit rect function from $[0, L]$, and $D = u_{\rm o}^{-1} - u_{\rm e}^{-1}$ is the dispersion coefficient of the nonlinear medium. It is through the $\mathcal{G}$-functions that spatiotemporal effects enter the quantum interference pattern. Details on the derivation of Eq. (45) can be found in Appendix A.

The collective interference term in Eq. (45) shows interesting behavior in certain limits of crystal separation. If the optical axes of the two crystals are parallel, the coincidence-count rate reduces to that from a single crystal of thickness $2L$ as $d \to 0$. Further, it reduces to that from a single crystal of thickness L as $d \to \infty$. We also note the absence of any shoulder modulation with τ, an important indication of the purity of the polarization Bell-state which is formed in postselection. In the case where the two crystals have equal thickness, the strongest interference occurs at delay $\tau = LD$. The visibility at this point is given by

$$V(LD) = 2\epsilon\frac{\rho}{1+\rho^2}\int_0^1 d\zeta\ \Re e\left[\mathcal{G}^{(12)}(\zeta;1)\right] \tag{46}$$

where $\zeta = z/L$ is a convenient dimensionless variable.

3. Small-Aperture Approximation

In the limit of very small apertures, no transverse wave vectors are allowed to propagate through the interferometer, and in the case of sufficiently thin bulk crystals and small separation distances, the quantum interference is effectively described by the conventionally used single-mode theory [18,22].

Figure 5 is a sketch illustrating how quantum interference arises in the interferometer of Fig. 4 assuming two identical crystals of thickness $L_1 = L_2 = L$, dispersion coefficient D, parallel optical axes, and both polarization analyzers set to 45°. In the limit of sufficiently small apertures, we may apply the conventional single-mode theory [22] and write the third term in Eq. (21) as the product of two probability amplitudes $A(t_\mathrm{A} - t_\mathrm{B})$ and $A^*(-t_\mathrm{A} + t_\mathrm{B})$, which slide back and forth across the $t_\mathrm{A} - t_\mathrm{B}$ axis as the relative optical-path delay τ is varied. In the diagonal portion of the illustration, these amplitudes are depicted by two grey-and-white rectangles. When the delay is set such that the two rectangles overlap, interference can be seen.

Within each rectangle, the white box represents the probability amplitude for detecting a photon pair produced in the first crystal, while the grey box represents the detection amplitude for a pair produced in the second. As the delay is set in the region $0 \leq \tau \leq LD/2$, the grey boxes overlap (shown as black) but the white boxes do not. In this regime, interference typical of a single crystal of thickness $2L$ is observed. As the delay is increased into the region $LD/2 \leq \tau \leq 3LD/2$, the photon pairs produced in the first crystal become indistinguishable with the photon pairs produced in the second crystal at the detection planes. As such, the probability amplitudes of detecting photon pairs produced in each each crystal exhibit collective interference. This is seen pictorially by the overlap of the grey boxes with the white boxes. Note that the two rectangles overlap completely at $\tau = LD$, the center of the region of interference. The interference visibility in this region depends on the phase shift between these two amplitudes, which is in turn dependent on spatial effects and the dispersion in the linear medium separating the crystals. As the distance d

between crystals is changed, the visibility in this region modulates sinusoidally between ± 1. As the delay is increased still further into the region $3LD/2 \leq \tau \leq 2LD$, the white boxes overlap (shown as light grey) but the grey ones do not, and we again return to the regime of single-crystal interference. In this way we can trace out the interference dip predicted by Eq. (45). This is illustrated in the inset at the lower right while representative experimental data is shown in the upper left inset. Figure 6 is similar to Fig. 5, but for the case of unequal crystal thicknesses $L_1 \neq L_2$.

In this small-aperture approximation, the dispersion-related $\mathcal{G}$-functions in Eq. (45) for the cases of parallel (p) and antiparallel (a) optical axes at $\tau/LD = 1$ are found in Appendix A to be

$$\mathcal{G}_{\mathrm{p}}^{(12)}(\zeta;1) = \exp(-i\Delta' d)\ \exp\left\{-i\frac{k_{\mathrm{p}}|\mathbf{M}L|^2}{8}\left[\frac{(\zeta-1)^2}{d_1} - \frac{(\zeta+1)^2}{d_1+d}\right]\right\} \tag{47}$$

and

$$\mathcal{G}_{\mathrm{a}}^{(12)}(\zeta;1) = \exp(-i\Delta' d)\ \exp\left\{-i\frac{k_{\mathrm{p}}|\mathbf{M}L|^2}{8}\left[\frac{(\zeta-1)^2}{d_1} - \frac{(\zeta-1)^2}{d_1+d}\right]\right\}, \tag{48}$$

where $k_{\mathrm{p}} = 2\pi/\lambda_{\mathrm{p}}$ and $|\mathbf{M}| = \frac{\partial}{\partial\theta_{\mathrm{e}}}\ln[n_{\mathrm{e}}(\omega_{\mathrm{p}}^0/2, \theta_{\mathrm{p}})]$ is the spatial walk-off vector [23].

When a plane wave pump is normally incident on thin crystals and the apertures are sufficiently small, the strictly collinear signal and idler beams are selected by the optical system, and no spatial effects due to transverse wave vectors can be observed. In this limit the dominant contribution to the phase between probability amplitudes arises from dispersion in the linear medium between the crystals [see Eqs. (47) and (48)]. For degenerate SPDC this phase term in air is [24]

$$\phi_{\mathrm{disp}}(d) \equiv \Delta' d = k_{\mathrm{p}}[n(\lambda_{\mathrm{p}}) - n(2\lambda_{\mathrm{p}})]\ d \sim \pi\ 0.059\ d[\mathrm{mm}] \tag{49}$$

where we have taken $\lambda_{\mathrm{p}} = 351.1$ nm in keeping with our experiments.

However, when long crystals are used, or the separation distance between the two crystals becomes large, some spatial effects due to transverse wave vectors become observable. The visibility at the center of the region of interference $tau = LD$ [Eq. (46)] for the case of parallel optical axes is given by

$$V_{\rm p}(LD) = 2\frac{d_1(d_1+d)}{d_1^2+(d_1+d)^2}\int_0^1 d\zeta\ \cos\left\{\frac{k_{\rm p}|\mathbf{M}L|^2}{2(d_1+d)}\left[(1+\zeta^2)\frac{d}{4d_1}-\zeta\left(1+\frac{d}{2d_1}\right)\right]+\phi_{\rm disp}(d)\right\}\,, \tag{50}$$

while for the case of antiparallel optical axes, it is given by

$$V_{\rm a}(LD) = -2\frac{d_1(d_1+d)}{d_1^2+(d_1+d)^2}\int_0^1 d\zeta\ \cos\left[\frac{k_{\rm p}|\mathbf{M}L|^2}{2(d_1+d)}\frac{d}{d_1}\left(\zeta-1\right)^2+\phi_{\rm disp}(d)\right]\,. \tag{51}$$

Furthermore, for small separation ($d \to 0$) between the two crystals with parallel optical axes, Eq. (46) becomes

$$V_{\rm p}(LD) = {\rm sinc}\left(\frac{k_{\rm p}}{2d_1}|\mathbf{M}L|^2\right) \tag{52}$$

as opposed to the unity value predicted by the single-mode theory. Note that this visibility is identical to that of a single crystal of thickness $2L$ as was shown in previous works [12]. Applying parameter values typical of our experiments, we find that if $d_1 = 1$ m, $\lambda_{\rm p} = 351.1$ nm and $|\mathbf{M}| = 0.07$, then $V_{\rm p} \sim {\rm sinc}(0.044\ L[{\rm mm}]^2)$. For these conditions, therefore, an observable deviation of $V_{\rm p}$ from unity can be realized only for sufficiently large crystal thicknesses.

In the case of antiparallel optical axes, the visibility at the center of the region of interference is

$$V_{\rm a}(LD) = -1\,, \tag{53}$$

which means that the coincidence-count rate is twice as high at the center as it is on the shoulders, assuming the analyzers are set so that $v_{\rm pol} = -1$ [see Eq. (43)]. In this case, the minus sign in Eq. (53) arises from a sign difference between the quadratic susceptibilities of the two crystals, and hence a sign difference between the spatial walkoff vectors $\mathbf{M}_1$ and $\mathbf{M}_2$. In effect, the spatial walkoff in one crystal compensates for the spatial walkoff in the other, and the spatial effects due to transverse wave vectors are cancelled out. Exploitation of this effect is common in the design of optical parametric oscillators.

The quantum state generated from SPDC, which is concurrently entangled in frequency and transverse wave vector, leads to transverse spatial effects that can be observed in quantum interference. As the aperture diameters are increased or the apertures are brought closer to the output plane of the nonlinear medium, a greater range of wave vectors is allowed to propagate through to the detectors. These transverse wave vectors introduce distinguishability between the signal and idler photons, thus reducing the visibility of the observed quantum interference. This is analogous to the temporal distinguishability introduced by the use of a femtosecond-pulsed pump.

Equation (45) is valid for any linear optical system. However, to enable swift evaluation of the integrals in this equation we approximate the circular apertures used in the experiments by "soft" Gaussian apertures of $(1/e)$ widths r_{A} and r_{B}. A sharp circular aperture, of the type used in experiments, has a diffraction pattern described by a first-order Bessel function, whereas a Gaussian aperture, of the type used in the numerical simulations, has a Gaussian diffraction pattern. Despite this fundamental difference, it is a fair approximation if the width r of the Gaussian is selected to roughly fit the width b of the Bessel function. In our calculations, this is done by choosing $r = b/2\sqrt{2}$. This approximation offers an indispensable advantage, as it allows us to evaluate the $\mathcal{G}$-functions analytically (see Appendix B) and thereby reduce the demand for numerical integration in making theoretical predictions. Under this approximation, an expression for the visibility function at $(\tau = LD)$ for parallel orientations of the optical axes is given by [see Appendix B and Eq. (26)]

$$V_{\mathrm{p}}(LD) = 2\frac{d_1(d_1+d)}{d_1^2+(d_1+d)^2}\frac{1}{\sqrt{1+\gamma^2}} \times \int_0^1 d\zeta\; e^{-\mathcal{B}\left(1-\zeta\frac{d}{d+2d_1}\right)^2} \cos\left[\mathcal{C}\zeta^2+\mathcal{D}\zeta+\mathcal{E}-\phi_\gamma(d)+\phi_{\mathrm{disp}}(d)\right] \tag{54}$$

where

$$\gamma = \frac{k_{\mathrm{p}} r^2}{4d_1}\frac{d}{d_1+d}\,, \qquad \phi_\gamma(d) = -\arctan(\gamma)\,, \tag{55}$$

and $r^2 = (r_{\rm A}^2 + r_{\rm B}^2)/2$. Here

$$\mathcal{B} = 2\left[\frac{k_{\rm p}|\mathbf{M}|Lr}{4(d_1+d)}\right]^2 \frac{1}{1+\gamma^2}\left(1+\frac{d}{2d_1}\right)^2 \tag{56}$$

$$\mathcal{C} = \frac{k_{\rm p}|\mathbf{M}L|^2}{8(d_1+d)}\frac{d}{d_1}\frac{1}{1+\gamma^2} \tag{57}$$

$$\mathcal{D} = -\frac{k_{\rm p}|\mathbf{M}L|^2}{2(d_1+d)}\left(1+\frac{d}{2d_1}\right)\frac{1}{1+\gamma^2} \tag{58}$$

$$\mathcal{E} = \frac{k_{\rm p}|\mathbf{M}L|^2}{8(d_1+d)}\left(\frac{d}{d_1} - 4\gamma^2\frac{d_1+d}{d}\right)\frac{1}{1+\gamma^2}. \tag{59}$$

Figure 7 presents a plot of the modulus of $V_{\rm p}(LD)$ given in Eq. (54) as a function of the crystal separation d for aperture diameters $b = 2.5$ mm, 4.0 mm, and 5.0 mm. Solid, shaded, and open circles denote the maxima of visibility and correspond to 2.5-mm, 4.0-mm, and 5.0-mm aperture diameters, respectively. For this plot, $L = 0.5$ mm, $\lambda_{\rm p} = 2\pi/k_{\rm p} = 351.1$ nm, and $|M| = 0.07$ in keeping with our experiments.

For antiparallel axes, the visibility function at $\tau = LD$ is

$$V_{\rm a}(LD) = -2\frac{d_1(d_1+d)}{d_1^2+(d_1+d)^2}\frac{1}{\sqrt{1+\gamma^2}} \times \int_0^1 d\zeta\; e^{-\mathcal{B}(1-\zeta)^2}\cos\left[\mathcal{E}(1-\zeta)^2 - \phi_\gamma(d) + \phi_{\rm disp}(d)\right]. \tag{60}$$

For the case of two crystals in contact ($d = 0$) we have $\mathcal{B} = 2(k_{\rm p}|\mathbf{M}|Lr/4d_1)^2$, $\mathcal{C} = 0$, $\mathcal{D} = -k_{\rm p}|\mathbf{M}L|^2/2d_1$, and $\mathcal{E} = 0$. From Eq. (54), we now observe that the visibility at $\tau = LD$ for parallel optical axes is

$$V_{\rm p}(LD) = \exp\left[-2\left(\frac{k_{\rm p}|\mathbf{M}|Lr}{4d_1}\right)^2\right]\;\mathrm{sinc}\left(\frac{k_{\rm p}}{2d_1}|\mathbf{M}L|^2\right) \tag{61}$$

while for antiparallel axes

$$V_{\rm a}(LD) = -\sqrt{2\pi}\,\frac{d_1}{k_{\rm p}|\mathbf{M}|Lr}\;\mathrm{erf}\left(\frac{k_{\rm p}|\mathbf{M}|Lr}{2\sqrt{2}d_1}\right). \tag{62}$$

Note that these visibilities depend on the aperture diameter, as well as the crystal thickness (as was seen in the previous section), and are once more markedly different from $V_{\rm a} = V_{\rm p} = 1$ as predicted by the single-mode theory. Equations (61) and (62) are plotted in Fig. 8 as a function of Gaussian aperture width r for three different crystal thicknesses $L = 0.5$ mm,

1.5 mm, and 5.0 mm. As predicted, the plot of the visibility obtained with a parallel orientation of the crystal axes (solid) reduces faster than the visibility for an antiparallel orientation (dashed).

III. EXPERIMENT

A. Experimental Arrangement

The experimental arrangement is illustrated in Fig. 9. A 200-mW cw Ar^+-ion laser operated at 351.1 nm served as the pump. This highly monochromatic laser beam was passed sequentially through a cascaded pair of β-barium-borate (BBO) crystals each with thickness 0.5 mm. The thickness of the air gap between the crystals was varied from $d =$ 2 mm to 100 mm. The crystals were aligned to produce pairs of orthogonally polarized photons in degenerate collinear type-II spontaneous parametric down-conversion ($\omega_{\rm s}^0 = \omega_{\rm i}^0 = \omega_{\rm p}^0/2$, where $\omega_{\rm s}^0$, $\omega_{\rm i}^0$, and $\omega_{\rm p}^0$ represent the central frequencies of the signal, idler, and pump fields, respectively). The laser power was sufficiently low to ensure, with high probability, that at most one photon pair was generated at a given time. The high visibility obtained from separate single-crystal quantum-interference experiments confirmed the validity of this assumption. A dichroic mirror, which transmits the 702-nm signal and idler beams while reflecting the 351-nm pump, was placed after the two crystals to remove residual pump laser beam.

The relative optical-path delay τ was introduced using a z-cut birefringent crystalline-quartz plate of variable thickness. The range of transverse wave vectors for the down-converted light was selected by circular apertures of diameters 2.5 mm to 5.0 mm. These apertures were positioned at 750 mm from the output plane of the second crystal. The single aperture used in the experimental setup is formally equivalent to the use of two apertures of identical diameters in the interferometer of Fig. 4, as used for the theoretical discussions of previous sections. The beams of down-converted light were then directed to a nonpolarizing

beam splitter, and thence to the two arms of a polarization intensity interferometer. Each arm of the interferometer comprised a Glan-Thompson polarization analyzer set at 45° with respect to the horizontal axis in the laboratory frame, establishing the basis for the polarization measurements. This basis was selected so as to permit observation of the quantum-interference pattern as a function of the optical-path delay τ. Finally, a convex lens (not shown in Fig. 9) was used to reduce the beam size to be less than the area of the detector, an actively quenched Peltier-cooled photon-counting avalanche photodiode. No spectral filters were used in any of the experiments. Coincidence detection was performed using a 3-nsec integration window and corrections for accidental coincidences were not necessary.

B. Experimental Results

First, we report quantum interference from crystals oriented with parallel and antiparallel optical axes in the small-aperture approximation. We demonstrate that the visibility at $\tau = LD$ varies sinusoidally with crystal separation d. Second, we investigate spatial effects on the visibility at $\tau = LD$ arising from the acceptance of a broader range of transverse wave vectors as the aperture is opened.

1. Parallel and Antiparallel Optical Axes

In this section we investigate the quantum interference patterns from SPDC in two identical crystals with parallel and antiparallel optical axes. The details of the experimental setup can be found in the previous section. The signal and idler fields were selected by a 2.5-mm circular aperture positioned 750 mm after the second crystal.

In the lower portion of Fig. 10, we plot the visibility function at the center of the interference region, $V(LD)$ as defined in Eq. (46), as a function of the separation d between the two 0.5-mm-thick BBO crystals. Each data point on the graph was obtained by calculating the ratio $(R_0 - R_{\rm int})/R_0$ where R_0 and $R_{\rm int}$ are the coincidence-count rates on the shoulders ($\tau < 0$ and $\tau > 2LD$) and at the center of the region of interference ($\tau = LD$), respectively.

The shaded circles plot the visibility at $\tau = LD$ as a function of crystal separation d when the optical axes of the two crystals are parallel. The open circles correspond to the case of antiparallel optical axes. As anticipated by Eqs. (54) and (60), the modulation in visibility with crystal separation is sinusoidal. The π-phase shift between these two cases arises from the change in sign of $\chi^{(2)}$ as the relative orientation of the optical axes is inverted. The theoretical curves (solid) are plots of Eqs. (54) and (60) assuming a Gaussian aperture of width r (defined as the diameter b of the circular apertures divided by $2\sqrt{2}$, the width at $1/e$), set to satisfy $2\sqrt{2}\,r = 2.5$ mm. The agreement of the theoretical curves with the experimental data demonstrates the validity of the Gaussian-aperture approximation. The remaining experimental parameters for this plot are $d_1 = 750$ mm, $\lambda_{\rm p} = 2\pi/k_{\rm p} = 351.1$ nm, and $|M| = 0.07$.

In the top left inset of Fig. 10, we show a representative example of quantum-interference patterns in which the visibility function $V_{\rm p}(LD)$ for crystals with parallel optical axes is either minimum or maximum. In the pattern exhibiting a peak (minimum), the crystals were 17.5 mm apart, while in the pattern exhibiting a dip (maximum) the crystals were 37.5 mm apart. Each data point presented on the visibility graph (lower inset) is extracted from such interference patterns. In the figure at the top right, where the two crystals are oriented with antiparallel optical axes, the opposite is true: the pattern exhibiting a dip (maximum) corresponds to a 17.5-mm crystal separation, while the pattern exhibiting a peak (minimum) corresponds to a 37.5-mm separation. Note from Eq. (44) that when both polarization analyzers are set to 45°, the polarization projection factor $v_{\rm pol} = -1$. Thus, from Eq. (43), positive values of $V(LD)$ correspond to a quantum interference dip while negative values correspond to a quantum interference peak. Orienting the crystals with antiparallel optical axes produces a sign difference between the second-order nonlinearities of the two crystals, so this condition is again reversed.

2. Spatiotemporal Effects

In previous work with single-crystal SPDC [12], we found that the acceptance of transverse wave vectors had substantial effects on quantum-interference patterns. To investigate spatiotemporal effects in dual-crystal SPDC, we carried out identical experiments to those detailed in the previous section, except that the 2.5-mm circular aperture was replaced with 4.0-mm and 5.0-mm circular apertures. The apertures remained positioned 750 mm from the output plane of the second crystal.

As with the single-crystal experiments, we found that increasing the diameter of the aperture lowers the visibility of the quantum interference patterns. This effect can be explained by considering the two independent mechanisms that introduce phases between the two-photon probability amplitudes for each crystal: 1) dispersion in the air separating the two crystals, which results in the phase ϕ_{disp} [Eq. (49)], and 2) the angular spread of down-converted light which results in the phase ϕ_γ [Eq. (55)]. Whereas ϕ_{disp} is dependent on the crystal separation d, but independent of r and d_1, ϕ_γ depends on all three parameters. However, when $d/d_1 \gg 1$, $\phi_\gamma \sim -\arctan(k_{\text{p}} r^2/4d_1)$. In this limit, ϕ_γ is dependent on r and d_1, but independent of the crystal separation d. As such, ϕ_γ dominates when the aperture is sufficiently large, while ϕ_{disp} dominates when the aperture is sufficiently small.

Fig. 11 displays plots of the visibility function at $\tau = LD$ as a function of the crystal separation d for 2.5-mm (top), 4.0-mm (middle), and 5.0-mm (bottom) aperture diameters. The two crystals are oriented with parallel axes. Note that for a fixed value of d, there is a reduction of visibility for increased aperture diameter. A reduction of visibility also occurs as the distance between the crystals is increased. Moreover, the period of oscillation contracts slightly as the aperture diameter is increased.

IV. CONCLUSION

We have developed a theory of Type-II spontaneous parametric down-conversion (SPDC) in media with inhomogeneous distributions of nonlinearity. The down-converted light can be concurrently entangled in frequency, wave vector, and polarization. We have shown that the state function of the down-converted light can be controlled by design of the nonlinearity profile in the crystal, as well as the spatial and spectral profile of the pump field. As one rudimentary design, we have considered the case of two nonlinear crystals separated by a linear dispersive medium. We anticipate that even greater control can be identified and exploited when other distributions of nonlinearity are employed.

The multiparameter formalism of SPDC in quantum interferometry [12] has been extended to incorporate the longitudinal nonlinearity profile of the medium. The quantum-interference pattern was shown to critically depend on the specific design of the nonlinearity profile. We studied the case of a cascaded pair of bulk crystals and experimentally verified the theoretical predictions. We have demonstrated that the quantum interference is sensitive to the medium between the crystals, as well as the design of the optical system for the down-converted light. In particular, collective interference effects were seen between the two probability amplitudes corresponding to detection of a photon pair generated in either crystal. The visibility of this collective interference between the two amplitudes depends on a relative phase, which is a function of the dispersion in the linear medium and the acceptance angle of the optical system. In the small-aperture approximation, we can continuously sweep the quantum-interference pattern from a high-visibility triangular dip to a high-visibility peak, simply by changing the distance between the two crystals. In principle, the same effect can also be observed when the dispersion properties of the linear medium are changed for a fixed distance between the crystals. Furthermore, as we increased the aperture diameter, and thus admitted a greater range of transverse wave vectors into the optical system, we observed a contraction in the oscillation period of the visibility.

Our findings are expected to be of interest to the development of SPDC sources using

multiple-crystal configurations and/or periodically poled materials, and to the advancement of quantum technologies through quantum-state engineering.

Acknowledgments.—This work was supported by the National Science Foundation, DARPA, and the David & Lucile Packard Foundation. The authors thank M. C. Booth for his invaluable help with the manuscript.

APPENDIX A: THE VISIBILITY FUNCTION $V(\tau)$

The purpose of this Appendix is to derive the visibility function $V(\tau)$ defined in Eq. (45). We consider the special case of degenerate collinear Type-II SPDC from two cascaded crystals of identical materials but different thicknesses. This source of SPDC is used in the interferometer shown in Fig. 4 with symmetric apertures and no spectral filters. Given this explicit configuration, we evaluate Eqs. (37), (38), (41), and (42) and rearrange the results to obtain Eq. (45).

To calculate $\mathcal{F}_{\rm AB}$ in Eq. (40), we need to consider the explicit form of the transfer function H for a given optical system. In the Fresnel approximation (which is well satisfied under the conditions of our experiments) the transfer functions H_i ($i = {\rm A}, {\rm B}$) in Eq. (40) are given by [12]

$$H_i(\mathbf{x}_i, \mathbf{q}; \omega) \propto \widetilde{f}(\omega)\, e^{{\rm i}\frac{\omega}{c}(d_1+d_2+f)}\; e^{-{\rm i}\frac{\omega}{2cf}|\mathbf{x}_i|^2\left(\frac{d_2}{f}-1\right)}\; e^{-{\rm i}\frac{cd_1}{2\omega}|\mathbf{q}|^2} \times \int d\mathbf{y}\; p_i(\mathbf{y})\; e^{-{\rm i}\left(\frac{\omega}{cf}\mathbf{x}_i-\mathbf{q}\right)\cdot\mathbf{y}} \tag{A1}$$

where $\widetilde{f}(\omega)$ is a (typically Gaussian) spectral filter profile, $\omega = \omega_{\rm p}^0/2 + \nu$ is the frequency of the degenerate SPDC, d_1 is the distance from the output plane of the second crystal to the aperture, d_2 is the distance between the aperture and each detector, f is the focal length of both lenses, and $p_i(\mathbf{y})$ is the pupil function for aperture $i = ({\rm A}, {\rm B})$. In the absence of interference filters [$\widetilde{f}(\omega) = 1$], the quasi-monochromatic field approximation ($\nu \ll \omega_{\rm p}^0$) allows the $\mathcal{F}_{\rm AB}$ functions in Eq. (40) to become frequency-independent, as shown in Eqs. (B3) and (B4).

The wave vector mismatch functions in Eq. (32) and (33) are given under these approximations by

$$\Delta\left(\mathbf{q},\nu\right) = -\nu D + \frac{2|\mathbf{q}|^2}{k_{\mathrm{p}}} + \mathbf{M}\cdot\mathbf{q} \tag{A2}$$

where Δ is the wave vector mismatch function due to dispersion in the crystals, and D and $\mathbf{M}$ are material properties of the crystals [22,23]. Here $D = u_{\mathrm{o}}^{-1} - u_{\mathrm{e}}^{-1}$ is the dispersion coefficient, where $u_{\mathrm{o,e}}$ are the group velocities for ordinary and extraordinary waves at the central frequency $\omega_{\mathrm{p}}^0/2$ and $\mathbf{q} = 0$ (i.e. $\theta_{\mathrm{e}} = \theta_{\mathrm{p}}$). In Eq. (A2), $\mathbf{M} = \frac{\partial}{\partial\theta_{\mathrm{e}}}\ln[n_{\mathrm{e}}(\omega_{\mathrm{p}}^0/2,\theta_{\mathrm{p}})]\mathbf{e}_{\mathrm{o.a.}}$ is the spatial walkoff vector, where $\mathbf{e}_{\mathrm{o.a.}}$ is a unit vector pointing in the direction of the optical axis.

Meanwhile, the dominant contribution to the dispersion function for the linear medium in Eq. (33) is

$$\Delta' = k_{\mathrm{p}} - K_{\mathrm{o}} - K_{\mathrm{e}} \tag{A3}$$

where $k_{\mathrm{p}} = n_{\mathrm{l}}(\omega_{\mathrm{p}}^0)\,\omega_{\mathrm{p}}^0/c$, $K_{\mathrm{e}} = n_{\mathrm{d}}(\omega_{\mathrm{e}})\,\omega_{\mathrm{e}}/c$ and $K_{\mathrm{o}} = n_{\mathrm{d}}(\omega_{\mathrm{o}})\,\omega_{\mathrm{o}}/c$ are the first-order expansions of k_{e} and k_{o}, and $n_{\mathrm{l}}(\omega)$ is the index of refraction in the linear medium. Evidently the dispersion in the linear medium between the two crystals simply contributes a difference in optical path length to the overall dispersion function. For a delay line of thickness l_τ, the phase functions $\eta_\tau(\mathbf{q},\nu)$ in Eq. (39) are given under the Fresnel and quasi-monochromatic field approximations by

$$\eta_\tau(\mathbf{q},\nu) = \left[-\nu D_\tau + \frac{2|\mathbf{q}|^2}{K_{\mathrm{p}}} + \mathbf{M}_\tau\cdot\mathbf{q} - K_{\mathrm{o}} - K_{\mathrm{e}}\right] l_\tau \tag{A4}$$

where D_τ and $\mathbf{M}_\tau$ are the dispersion coefficient and the spatial walkoff vector for the birefringent material of the delay line, respectively. If we consider the contribution $\mathrm{e}^{-\mathrm{i}\eta_\tau(\mathbf{q},\nu)}$ for the delay line along with Equation (32), we obtain

$$\tilde{\chi}_r^{(2)}(\mathbf{q},\nu)\;\mathrm{e}^{-\mathrm{i}\eta_\tau(\mathbf{q},\nu)} = e^{-\mathrm{i}\Delta' d\,\delta_{r,1}}\int_{-L_r}^{0} dz\;\mathcal{Q}_r(\nu;z)\;\mathcal{M}_r(\mathbf{q};z) \tag{A5}$$

for $r = (1,2)$ where $\tilde{\chi}_1^{(2)}(\mathbf{q},\nu)$ and $\tilde{\chi}_2^{(2)}(\mathbf{q},\nu)$ are the nonlinearity profiles of the first and second crystals, respectively. We have here introduced the quantities

$$\mathcal{M}_r(\mathbf{q};z) = e^{\mathrm{i}(\mathbf{M}_r z - \boldsymbol{\mathcal{L}}_r)\cdot\mathbf{q}}\; e^{2\mathrm{i}\frac{z-\beta_r}{K_\mathrm{p}}|\mathbf{q}|^2} \tag{A6}$$

$$\mathcal{Q}_r(\nu;z) = e^{-\mathrm{i}\nu(D_r z + \tau_r)} \tag{A7}$$

where the parameters

$$\tau_r = \tau - L_2 D \cdot \delta_{r,1} \tag{A8}$$

$$\beta_r = l_\tau + (L_2 + d)\cdot\delta_{r,1} \tag{A9}$$

$$\boldsymbol{\mathcal{L}}_r = \mathbf{M}_\tau l_\tau + \mathbf{M}_2 L_{3-r}\cdot\delta_{r,1} \tag{A10}$$

for $r = (1,2)$ and where $\tau = -l_\tau D_\tau$. Under these conditions the single crystal components of the coincidence-count rate are then given by

$$R_0^{(r)} = \frac{\mu^2_{\mathrm{Ao,Be}} + \mu^2_{\mathrm{Bo,Ae}}}{D}\int dz\; \Pi^2_{L_r}(z)\; \mathcal{I}[-(\mathbf{M}_r z + \boldsymbol{\mathcal{L}}_r), \mathbf{0}, s_r, s_r] \tag{A11}$$

and

$$R_{\mathrm{int}}^{(r)} = 2\frac{\mu_{\mathrm{Ao,Be}}\;\mu_{\mathrm{Bo,Ae}}}{D}\int dz\; \Pi_{L_r}(z)\; \Pi_{L_r}\left(\frac{2\tau_r}{D} - z\right)\; \mathcal{I}[-(\mathbf{M}_r z + \boldsymbol{\mathcal{L}}_r), \boldsymbol{\mathcal{Z}}_r, s_r, s_r] \tag{A12}$$

where for brevity we introduce $\Pi_{L_r}(z) \equiv \mathrm{rect}_{[0,L_r]}(z)$. Here the distance $s_r = d_1 - z + \beta_r$,

$$\boldsymbol{\mathcal{Z}}_r = -2\left(\mathbf{M}_r\frac{\tau_r}{D} + \boldsymbol{\mathcal{L}}_r\right), \tag{A13}$$

and

$$\mathcal{I}\left[\mathbf{z}_0(z), \mathbf{Z}(z,z'), s_k, s_n\right] = \int\; d\mathbf{q}\; d\mathbf{q}'\, \mathcal{M}_k(\mathbf{q};z)\mathcal{M}^*_n(\mathbf{q}';z')\; \mathcal{F}_{\mathrm{AB}}(\mathbf{q}, \pm\mathbf{q}', \nu)\,. \tag{A14}$$

We have assumed, in keeping with our experiments, apertures which are symmetric such that $|p_{\mathrm{A,B}}(\mathbf{y})| = |p_{\mathrm{A,B}}(-\mathbf{y})|$. Further details of $\mathcal{F}_{\mathrm{AB}}(\mathbf{q}, \pm\mathbf{q}', \nu)$ can be found in Appendix B. In experimental practice, the distance d_1 between the output plane of the second crystal and the aperture is much longer than the crystal thicknesses L_1 and L_2 and the optical path length l_τ of the delay line. As such, we may assume that

$$s_r = d_1 - z + \beta_r \sim d_1 + (2-r)d. \tag{A15}$$

Also note that there are no approximations constraining the value of d.

The baseline coincidence-count rate from collective interference between the amplitudes from the two crystals is given by

$$\begin{aligned} R_0^{(12)} &= \epsilon \frac{\mu_{\mathrm{Ao,Be}}^2 + \mu_{\mathrm{Bo,Ae}}^2}{D} \\ &\times \left\{ \int dz\ \Pi_{L_1}(z)\ \Pi_{L_2}\left(z - \frac{\tau_1 - \tau_2}{D}\right)\ \mathcal{I}[-(\mathbf{M}_1 z + \boldsymbol{\mathcal{L}}_1), \boldsymbol{\mathcal{Z}}_{12}^0(z), s_1, s_2]\ e^{-\mathrm{i}\Delta' d} + \right. \\ &+ \left. \int dz\ \Pi_{L_2}(z)\ \ \Pi_{L_1}\left(z - \frac{\tau_2 - \tau_1}{D}\right)\ \mathcal{I}[-(\mathbf{M}_2 z + \boldsymbol{\mathcal{L}}_2), \boldsymbol{\mathcal{Z}}_{21}^0(z), s_2, s_1]\ e^{\mathrm{i}\Delta' d} \right\} \end{aligned} \tag{A16}$$

where

$$\boldsymbol{\mathcal{Z}}_{12}^0(z) = -\left[z\,(\mathbf{M}_1 - \mathbf{M}_2) + \mathbf{M}_2 \frac{\tau_1 - \tau_2}{D} + \boldsymbol{\mathcal{L}}_1 - \boldsymbol{\mathcal{L}}_2 \right] \tag{A17}$$

and the remaining parameters are given by

$$\tau_1 = \tau - L_2 D \qquad s_1 = d_1 + d \qquad \boldsymbol{\mathcal{L}}_1 = \mathbf{M}_\tau l_\tau + \mathbf{M}_2 L_2 \tag{A18}$$

$$\tau_2 = \tau \qquad\qquad s_2 = d_1 \qquad\qquad \boldsymbol{\mathcal{L}}_2 = \mathbf{M}_\tau l_\tau\,. \tag{A19}$$

It is important to note that $R_0^{(12)} = 0$ for all values of τ, since in this case $\tau_1 - \tau_2 = -LD_2$ and the two rectangular functions $\Pi_{L_r}(z)$ in Eq. (A16) never actually overlap. Thus the coincidence-count rates are strictly constant outside the region of interference. This lack of shoulder modulation is an important indicator of the purity of the observed polarization-entangled two-photon state. The collective interference term itself is given by

$$\begin{aligned} R_{\mathrm{int}}^{(12)} &= 2\epsilon \frac{\mu_{Ao,Be}\ \mu_{Bo,Ae}}{D} \\ &\times \left\{ \int dz\ \Pi_{L_1}(z)\ \Pi_{L_2}\left(\frac{\tau_1 + \tau_2}{D} - z\right)\ \mathcal{I}[-(\mathbf{M}_1 z + \boldsymbol{\mathcal{L}}_1), \boldsymbol{\mathcal{Z}}_{12}^{\mathrm{int}}(z), s_1, s_2]\ e^{-\mathrm{i}\Delta' d} + \right. \\ &+ \left. \int dz\ \Pi_{L_2}(z)\ \ \Pi_{L_1}\left(\frac{\tau_2 + \tau_1}{D} - z\right)\ \mathcal{I}[-(\mathbf{M}_2 z + \boldsymbol{\mathcal{L}}_2), \boldsymbol{\mathcal{Z}}_{21}^{\mathrm{int}}(z), s_2, s_1]\ e^{\mathrm{i}\Delta' d} \right\} \end{aligned} \tag{A20}$$

with

$$\boldsymbol{\mathcal{Z}}_{12}^{\mathrm{int}}(z) = -\left[z\,(\mathbf{M}_1 - \mathbf{M}_2) + \mathbf{M}_2 \frac{\tau_1 + \tau_2}{D} + \boldsymbol{\mathcal{L}}_1 + \boldsymbol{\mathcal{L}}_2 \right] \tag{A21}$$

where $\boldsymbol{\mathcal{Z}}_{21}^{0,\mathrm{int}}$ can be found by interchanging all indices $(1 \leftrightarrow 2)$ in $\boldsymbol{\mathcal{Z}}_{12}^{0,\mathrm{int}}$.

With sufficient algebra, it is possible to arrange all of the contributions to the coincidence rate in Eqs. (A11), (A12), (A16) and (A20) to obtain the structure of Eq. (43), where the baseline coincidence-count rate is given by

$$R_0 = \left(\frac{k_{\rm p}}{2}\right)^2 \left[\frac{L_1}{Ds_1^2} + \frac{L_2}{Ds_2^2}\right] \tilde{P}_{\rm A}(\mathbf{0})\ \tilde{P}_{\rm B}(\mathbf{0})\,, \tag{A22}$$

where $\tilde{P}_i(\mathbf{q})$ is given by Eq. (B4), and the polarization analyzer projection factor is

$$v_{\rm pol} = 2\frac{\mu_{\rm Ao,Be}\ \mu_{\rm Bo,Ae}}{\mu_{\rm Ao,Be}^2 + \mu_{\rm Bo,Ae}^2}\,. \tag{A23}$$

This, in turn, leads to Eq. (45), the desired visibility function in the special case where $L_1 = L_2 = L$:

$$\begin{aligned} V(\tau) = & \frac{1}{1+\rho^2}\int dz\ \Pi_L(z)\ \Pi_L\left(\frac{2\tau}{D} - 2L - z\right)\ \mathcal{G}^{(1)}\left(\frac{z}{L};\frac{\tau}{LD}\right) \\ & + \frac{1}{1+\rho^2}\int dz\ \Pi_L(z)\ \Pi_L\left(\frac{2\tau}{D} - z\right)\ \mathcal{G}^{(2)}\left(\frac{z}{L};\frac{\tau}{LD}\right) \\ & + 2\epsilon\frac{\rho}{1+\rho^2}\int dz\ \Pi_L(z)\ \Pi_L\left(\frac{2\tau}{D} - L - z\right)\ \Re e\left[\mathcal{G}^{(12)}\left(\frac{z}{L}+\frac{1}{2};\frac{\tau}{LD}\right)\ e^{-{\rm i}\Delta' d}\right]\,. \end{aligned} \tag{A24}$$

Here the functions $\mathcal{G}_{r=1,2}$ are given by

$$\mathcal{G}^{(r)}\left(\frac{z}{L};\frac{\tau}{LD}\right) = \mathcal{N}\left[-(\mathbf{M}_r z + \boldsymbol{\mathcal{L}}_r), \boldsymbol{\mathcal{Z}}_r, s_r, s_r\right] \tag{A25}$$

for the single-crystal contributions, while the component due to collective interference is given by

$$\mathcal{G}^{(12)}\left(\frac{z}{L}+\frac{1}{2};\frac{\tau}{LD}\right) = \mathcal{N}\left[-(\mathbf{M}_1 z + \boldsymbol{\mathcal{L}}_1), \boldsymbol{\mathcal{Z}}_{12}^0(z), s_1, s_2\right]\,. \tag{A26}$$

The function $\mathcal{N}$ is defined in Appendix B by Eq. (B9), while the normalization factor is given by $\rho = (d_1 + d)/d_1$.

For a delay line comprised of a thin z-cut birefringent element such as quartz, $\mathbf{M}_\tau = \mathbf{0}$ and

$$\boldsymbol{\mathcal{L}}_1 = \mathbf{M}_2 L_2\,, \qquad\qquad \boldsymbol{\mathcal{L}}_2 = \mathbf{0}\,. \tag{A27}$$

Under this assumption there are two important limits: large separation between the crystals ($d \to \infty$) and contact between the crystals ($d \to 0$). When the two crystals are moved very

far apart, we expect interference from SPDC to be governed only by the second crystal, and the quantum-interference pattern to be identical to that of SPDC from a single crystal of thickness L_2. This can be seen from Eq. (A24) by noting that in this case the normalization factor $\rho \to \infty$ and only the last of the three integrals in Eq. (A24) survives. In this limit

$$V_{d\to\infty}(\tau) = \frac{1}{L}\int dz\ \Pi_L(z)\ \Pi_L\left(\frac{2\tau}{D} - z\right)\ \mathcal{G}^{(2)}\left(\frac{z}{L}; \frac{\tau}{LD}\right) \tag{A28}$$

and the shoulder normalization factor (A22) is identical to that of a single crystal of thickness L. When two crystals of the same material with parallel optical axes are in contact, the quantum interference pattern is identical to that obtained from a single crystal of thickness $2L$. However, note that this does not hold for antiparallel orientations of the optical axes of the two crystals.

1. Parallel Optical Axes

If the crystals are oriented such that their optical axes are parallel, $\mathbf{M}_1 = \mathbf{M}_2 = \mathbf{M}$ and the $\mathcal{G}$ functions in Eq. (45) are specified by

$$\mathcal{G}_{\mathrm{p}}^{(1)}(\zeta; x) = \mathcal{N}\left[-\mathbf{M}L(\zeta + x), -2\mathbf{M}Lx, d_1 + d, d_1 + d\right] \tag{A29}$$

$$\mathcal{G}_{\mathrm{p}}^{(12)}(\zeta; x) = \mathcal{N}\left[-\mathbf{M}L(\zeta + x), -2\mathbf{M}Lx, d_1 + d, d_1\right] \tag{A30}$$

$$\mathcal{G}_{\mathrm{p}}^{(2)}(\zeta; x) = \mathcal{N}\left[-\mathbf{M}L(\zeta + x), -2\mathbf{M}Lx, d_1, d_1\right] \tag{A31}$$

where $\zeta = z/L$, $x = \tau/LD$, and $\mathcal{N}$ is defined in Eq. (B9).

2. Antiparallel Optical Axes

The antiparallel orientation of the optical axes of the two crystals gives $\mathbf{M}_1 = -\mathbf{M}_2 = \mathbf{M}$ and the $\mathcal{G}$-functions are specified by

$$\mathcal{G}_{\mathrm{a}}^{(1)}(\zeta; x) = \mathcal{N}\left[-\mathbf{M}L(\zeta + x - 2), -2\mathbf{M}L(x - 1), d_1 + d, d_1 + d\right] \tag{A32}$$

$$\mathcal{G}_{\mathrm{a}}^{(12)}(\zeta; x) = \mathcal{N}\left[-\mathbf{M}L(\zeta + x - 2), -2\mathbf{M}L(\zeta - 1), d_1 + d, d_1\right] \tag{A33}$$

$$\mathcal{G}_{\mathrm{a}}^{(2)}(\zeta; x) = \mathcal{N}\left[\mathbf{M}L(\zeta + x), 2\mathbf{M}Lx, d_1, d_1\right]. \tag{A34}$$

APPENDIX B: THE FUNCTION $\mathcal{N}$

In this Appendix, we derive an explicit form of the function $\mathcal{N}$, which appears in Eq. (A25). We define

$$\mathcal{N}(\mathbf{z}_0, \mathbf{Z}, s_k, s_n) = \frac{s_k s_n}{(k_\mathrm{p}/2)^2} \frac{\mathcal{I}(\mathbf{z}_0, \mathbf{Z}, s_k, s_n)}{\tilde{P}_\mathrm{A}(0)\tilde{P}_\mathrm{B}(0)} \tag{B1}$$

where $\tilde{P}_i(\mathbf{q})$, $k, n = (1, 2)$, s_1 and s_2 are defined in Eqs. (A18), and

$$\mathcal{I}\left[\mathbf{z}_0(z), \mathbf{Z}(z, z'), s_k, s_n\right] = \int d\mathbf{q}\; d\mathbf{q}'\, \mathcal{M}_k(\mathbf{q}; z)\mathcal{M}_n^*(\mathbf{q}'; z')\; \mathcal{F}_\mathrm{AB}(\mathbf{q}, \pm\mathbf{q}', \nu)\,, \tag{B2}$$

where $\mathcal{M}_r$ is defined in Eq. (A6). The function $\mathcal{F}_\mathrm{AB}$, defined by Eq. (40), under the Fresnel approximation and in the absence of interference filters takes the form

$$\mathcal{F}_\mathrm{AB}(\mathbf{q}, \pm\mathbf{q}', \nu) = \tilde{P}_\mathrm{A}(\mathbf{q} \mp \mathbf{q}')\; \tilde{P}_\mathrm{B}(-\mathbf{q} \pm \mathbf{q}')\; e^{-\mathrm{i}\frac{2d_1(\nu)}{k_\mathrm{p}}\left(|\mathbf{q}|^2 - |\mathbf{q}'|^2\right)}\,. \tag{B3}$$

Here

$$\tilde{P}_i(\mathbf{q}) = \int d\mathbf{y}\; p_i(\mathbf{y})p_i^*(\mathbf{y})\; e^{-\mathrm{i}\mathbf{y}\cdot\mathbf{q}} \tag{B4}$$

$$d_1(\nu) = d_1\left[1 - \left(\frac{2\nu}{\omega_\mathrm{p}^0}\right)^2\right]^{-1} \tag{B5}$$

for $i = (\mathrm{A}, \mathrm{B})$. Given these explicit forms, Eq. (B2) becomes

$$\mathcal{I}(\mathbf{z}_0, \mathbf{Z}, s_k, s_n) = \frac{(k_\mathrm{p}/2)^2}{s_k s_n}\; \exp\left[-\mathrm{i}\frac{k_\mathrm{p}}{8s_n}|\mathbf{Z}|^2\right] \int d\mathbf{q}\; \tilde{P}_\mathrm{A}(-\mathbf{q})\; \tilde{P}_\mathrm{B}(\mathbf{q})\; \mathcal{W}\left(\mathbf{q} + \frac{k_\mathrm{p}}{4s_n}\mathbf{Z}\right)\; e^{-\mathrm{i}\mathbf{q}\cdot\mathbf{z}_0} \tag{B6}$$

where

$$\mathcal{W}(\mathbf{q}) = -\frac{2\mathrm{i}d_r^{(kn)}}{\pi k_\mathrm{p}} \exp\left[\frac{2\mathrm{i}d_r^{(kn)}}{k_\mathrm{p}}|\mathbf{q}|^2\right] \tag{B7}$$

with

$$\frac{1}{d_r^{(kn)}} = \frac{1}{s_n} - \frac{1}{s_k}. \tag{B8}$$

Finally, using Eq. (B6) we obtain

$$\mathcal{N}(\mathbf{z}_0, \mathbf{Z}, s_k, s_n) = \exp\left[-\mathrm{i}\frac{k_\mathrm{p}}{8s_n}|\mathbf{Z}|^2\right] \int d\mathbf{q}\, \tilde{\mathcal{P}}_\mathrm{A}(-\mathbf{q})\, \tilde{\mathcal{P}}_\mathrm{B}(\mathbf{q})\, \mathcal{W}\left(\mathbf{q} + \frac{k_\mathrm{p}}{4s_n}\mathbf{Z}\right) e^{-\mathrm{i}\mathbf{q}\cdot\mathbf{z}_0} \tag{B9}$$

with $\tilde{\mathcal{P}}_i(\mathbf{q}) = \tilde{P}_i(\mathbf{q})/\tilde{P}_i(\mathbf{0})$ for $i = \mathrm{A}, \mathrm{B}$. In the limit $s_k \to s_n$, Eq. (B9) becomes

$$\mathcal{N}(\mathbf{z}_0, \mathbf{Z}, s_n, s_n) = \exp\left[-\mathrm{i}\frac{k_\mathrm{p}}{8s_n}|\mathbf{Z}|^2\right] \tilde{\mathcal{P}}_\mathrm{A}\left(\frac{k_\mathrm{p}}{4s_n}\mathbf{Z}\right) \tilde{\mathcal{P}}_\mathrm{B}\left(-\frac{k_\mathrm{p}}{4s_n}\mathbf{Z}\right) e^{\mathrm{i}\frac{k_\mathrm{p}}{4s_n}\mathbf{Z}\cdot\mathbf{z}_0}\,. \tag{B10}$$

1. Small-Aperture Approximation

Suppose that the apertures are so small that the pupil functions $p_{\mathrm{A,B}}(\mathbf{y})$ may be treated as delta functions at $\mathbf{y} = 0$. In this case, $\tilde{\mathcal{P}}_\mathrm{A}(\mathbf{q})$ is a constant and Eq. (B9) becomes

$$\mathcal{N}_\mathrm{SM}(\mathbf{z}_0, \mathbf{Z}, s_k, s_n) = \exp\left[-\mathrm{i}\frac{k_\mathrm{p}}{8}\left(\frac{|\mathbf{Z} - \mathbf{z}_0|^2}{s_n} - \frac{|\mathbf{z}_0|^2}{s_k}\right)\right]. \tag{B11}$$

In the limit $s_k \to s_n$ we then have

$$\mathcal{N}_\mathrm{SM}(\mathbf{z}_0, \mathbf{Z}, s_n, s_n) = \exp\left[-\mathrm{i}\frac{k_\mathrm{p}}{8s_n}\left(|\mathbf{Z} - \mathbf{z}_0|^2 - |\mathbf{z}_0|^2\right)\right]. \tag{B12}$$

2. Gaussian-Aperture Approximation

To simplify the analysis, we consider the case of Gaussian apertures with $p_i(\mathbf{y}) = \exp(-|\mathbf{y}|^2/2r_i^2)$ and $\tilde{\mathcal{P}}_i(\mathbf{q}) = \exp(-|\mathbf{q}|^2 r_i/4)$, so that

$$\begin{aligned}\mathcal{N}_\mathrm{G}(\mathbf{z}_0, \mathbf{Z}, s_k, s_n) = \frac{1 - i\gamma}{1 + \gamma^2}\, &\exp\left[\mathrm{i}\frac{k_\mathrm{p}}{8(s_k - s_n)}|\mathbf{Z}|^2\right] \\ &\times \exp\left[-\mathrm{i}\frac{k_\mathrm{p}}{8d_r^{(kn)}}\frac{1 - i\gamma}{1 + \gamma^2}\left|\mathbf{z}_0 - \frac{s_k}{s_k - s_n}\mathbf{Z}\right|^2\right]\end{aligned} \tag{B13}$$

where

$$\gamma = \frac{k_\mathrm{p}}{4d_r^{(kn)}}\frac{r_\mathrm{A}^2 + r_\mathrm{B}^2}{2}. \tag{B14}$$

It is useful to write the complex constant

$$\frac{1 - i\gamma}{1 + \gamma^2} = \frac{1}{\sqrt{1 + \gamma^2}}\, e^{-\mathrm{i}\arctan\gamma} \tag{B15}$$

so that we may write the phase

$$\phi_\gamma = -\arctan\left(\frac{k_\mathrm{p}}{4d_1}\frac{r_\mathrm{A}^2+r_\mathrm{B}^2}{2}\frac{d/d_1}{1+d/d_1}\right). \tag{B16}$$

In summary, the $\mathcal{N}$-function in the Gaussian-aperture approximation is given by

$$\begin{aligned}\mathcal{N}_\mathrm{G}(\mathbf{z}_0,\mathbf{Z},s_k,s_n) = \frac{1}{\sqrt{1+\gamma^2}}\ \exp\left[-\frac{k_\mathrm{p}}{8d_r^{(kn)}}\frac{\gamma}{1+\gamma^2}\left|\mathbf{z}_0-\frac{s_k}{s_k-s_n}\mathbf{Z}\right|^2\right]\\ \times\ \exp\left[-\mathrm{i}\frac{k_\mathrm{p}}{8d_r^{(kn)}}\frac{1}{1+\gamma^2}\left|\mathbf{z}_0-\frac{s_k}{s_k-s_n}\mathbf{Z}\right|^2\right]\\ \times\ \exp\left[\mathrm{i}\frac{k_\mathrm{p}}{8(s_k-s_n)}|\mathbf{Z}|^2+\mathrm{i}\phi_\gamma\right].\end{aligned} \tag{B17}$$

In the limit $s_k \to s_n$, we have

$$\begin{aligned}\mathcal{N}_\mathrm{G}(\mathbf{z}_0,\mathbf{Z},s_n,s_n) = \exp\left[-\left|\frac{k_\mathrm{p}\mathbf{Z}}{4s_n}\right|^2\frac{r_\mathrm{A}^2+r_\mathrm{B}^2}{4}\right]\\ \times\ \exp\left[-\mathrm{i}\frac{k_\mathrm{p}}{8s_n}\left(|\mathbf{Z}-\mathbf{z}_0|^2-|\mathbf{z}_0|^2\right)\right].\end{aligned} \tag{B18}$$

REFERENCES

[1] S. E. Harris, M. K. Oshman, and R. L. Byer, Phys. Rev. Lett. **18,** 732 (1967); D. Magde and H. Mahr, Phys. Rev. Lett. **18,** 905 (1967); D. N. Klyshko, *Photons and Nonlinear Optics* (Nauka, Moscow, 1980); J. Peřina, Z. Hradil, and B. Jurčo, *Quantum Optics and Fundamentals of Physics* (Kluwer, Boston, 1994); L. Mandel and E. Wolf, *Optical Coherence and Quantum Optics* (Cambridge, New York, 1995), Ch. 22.

[2] J. S. Bell, Physics **1**, 195 (1964); J. F. Clauser, M. A. Horne, A. Shimony, and R. A. Holt, Phys. Rev. Lett. **23,** 880 (1969); P. G. Kwiat, K. Mattle, H. Weinfurter, A. Zeilinger, A. V. Sergienko, and Y. H. Shih, Phys. Rev. Lett. **75,** 4337 (1995).

[3] L. Hardy, Phys. Rev. Lett. **71,** 1665 (1993); J. R. Torgesson, D. Branning, C.H. Monken, and L. Mandel, Phys. Lett. A, **204,** 323 (1995); G. Di Giuseppe, F. De Martini, and D. Boschi, Phys. Rev. A **56,** 176 (1997); D. Boschi, S. Branca, F. De Martini, and L. Hardy, Phys. Rev. Lett. **79,** 2755 (1997); A. G. White, D. F. V. James, P. H. Eberhard, and P. G. Kwiat, Phys. Rev. Lett. **83,** 3103 (1999).

[4] D. M. Greenberger, M. A. Horne, and A. Zeilinger, in *Bell's Theorem, Quantum Theory, and Conceptions of the Universe*, edited by M. Kafatos (Kluwer, Dordrecht, 1989); D. M. Greenberger, M. A. Horne, A. Shimony, and A. Zeilinger, Am. J. Phys. **58,** 1131 (1990); D. Bouwmeester, J.-W. Pan, M. Daniell, H. Weinfurter, and A. Zeilinger, Phys. Rev. Lett. **82,** 1345 (1999).

[5] D. N. Klyshko, Sov. J. Quantum Electron. **7,** 591 (1977); A. Migdall, R. Datla, A. V. Sergienko, J. S. Orszak, and Y. H. Shih, Appl. Opt. **37,** 3455 (1998).

[6] B. E. A. Saleh, B. M. Jost, H.-B. Fei, and M. C. Teich, Phys. Rev. Lett. **80,** 3483 (1998); H.-B. Fei, B. M. Jost, S. Popescu, B. E. A. Saleh, and M. C. Teich, Phys. Rev. Lett. **78,** 1679 (1997).

[7] B. M. Jost, A. V. Sergienko, A. F. Abouraddy, B. E. A. Saleh, and M. C. Teich, Opt.

Express **3,** 81 (1998); B. E. A. Saleh, A. F. Abouraddy, A. V. Sergienko, and M. C. Teich, Phys. Rev. A **62,** 043816 (2000); A. F. Abouraddy, B. E. A. Saleh, A. V. Sergienko, and M. C. Teich, Phys. Rev. Lett. **87,** 123602-1 (2001); A. F. Abouraddy, B. E. A. Saleh, A. V. Sergienko, and M. C. Teich, Opt. Express **9,** 498 (2001); A. F. Abouraddy, B. E. A. Saleh, A. V. Sergienko, and M. C. Teich, J. Opt. Soc. Am. B **19,** in press (2002); L. A. Lugiato, A. Gatti, and E. Brambilla, J. Opt. B, in press (2002).

[8] A. K. Ekert, Phys. Rev. Lett. **67,** 661 (1991); J. G. Rarity and P. R. Tapster, Phys. Rev. A **45,** 2052 (1992); J. Brendel, N. Gisin, W. Tittel, and H. Zbinden, Phys. Rev. Lett. **82,** 2594 (1999); A. V. Sergienko, M. Atatüre, Z. Walton, G. Jaeger, B. E. A. Saleh, and M. C. Teich, Phys. Rev. A **60,** R2622 (1999).

[9] C. H. Bennett, G. Brassard, C. Crepeau, R. Jozsa, A. Peres, and W. K. Wootters, Phys. Rev. Lett. **70,** 1895 (1993); D. Boschi, S. Branca, F. De Martini, L. Hardy, and S. Popescu, Phys. Rev. Lett. **80,** 1121 (1998); D. Bouwmeester, J.-W. Pan, K. Mattle, M. Eibl, H. Weinfurter, and A. Zeilinger, Nature **390,** 575 (1997).

[10] G. Di Giuseppe, L. Haiberger, F. De Martini, and A. V. Sergienko, Phys. Rev. A **56,** R21 (1997); W. P. Grice, R. Erdmann, I. A. Walmsley, and D. Branning, Phys. Rev. A **57,** R2289 (1998); W. P. Grice and I. A. Walmsley, Phys. Rev. A **56,** 1627 (1997); T. E. Keller and M. H. Rubin, Phys. Rev. A **56,** 1534 (1997); J. Peřina, Jr., A. V. Sergienko, B. M. Jost, B. E. A. Saleh, and M. C. Teich, Phys. Rev. A **59,** 2359 (1999); D. Branning, W. P. Grice, R. Erdmann, and I. A. Walmsley, Phys. Rev. Lett. **83,** 955 (1999); T. Tsegaye, J. Söderholm, M. Atatüre, A. Trifonov, G. Björk, A. V. Sergienko, B. E. A. Saleh, and M. C. Teich, Phys. Rev. Lett. **85,** 5013 (2000).

[11] M. Atatüre, A. V. Sergienko, B. M. Jost, B. E. A. Saleh, and M. C. Teich, Phys. Rev. Lett. **83,** 1323 (1999); M. Atatüre, A. V. Sergienko, B. E. A. Saleh, and M. C. Teich, Phys. Rev. Lett. **84,** 618 (2000).

[12] M. Atatüre, G. Di Giuseppe, M. D. Shaw, A. V. Sergienko, B. E. A. Saleh, and M.

C. Teich, Phys. Rev. A, in press (February 2002); M. Atatüre, G. Di Giuseppe, M. D. Shaw, A. V. Sergienko, B. E. A. Saleh, and M. C. Teich, submitted to Phys. Rev. A.

[13] X. Y. Zhou, L. J. Wang, and L. Mandel, Phys. Rev. Lett. **67,** 318 (1991).

[14] D. N. Klyshko, Zh. Eksp. Teor. Fiz. **104**, 2676 (1993) [JETP **77**, 222 (1993)]; D. N. Klyshko, Laser Physics **4**, 663 (1994); A. V. Burlakov, M. V. Chekhova, D. N. Klyshko, S. P. Kulik, A. N. Penin, Y. H. Shih and D. V. Strekalov, Phys. Rev. A **56**, 3214 (1997); A. V. Burlakov, D. N. Klyshko, S. P. Kulik, A. N. Penin and M. V. Chekhova, Pis'ma Zh. Eksp. Teor. Fiz. **65**, 20 (1997) [JETP Lett. **65**, 19 (1997)].

[15] T. J. Herzog, J. G. Rarity, H. Weinfurter, and A. Zeilinger, Phys. Rev. Lett. **72,** 629 (1994); T. J. Herzog, P.G. Kwiat, H. Weinfurter, and A. Zeilinger, Phys. Rev. Lett. **75,** 3024 (1995); P. W. Milonni, H. Fearn, and A. Zeilinger, Phys. Rev. A. **53,** 4556 (1996).

[16] J.W. Pan, D. Bouwmeester, H. Weinfurter, and A. Zeilinger, Phys. Rev. Lett. **80,** 3891 (1998); D. Bouwmeester, J.-W. Pan, M. Daniell, H. Weinfurter, and A. Zeilinger, Phys. Rev. Lett. **82,** 1345 (1999); D. Branning, W. Grice, R. Erdmann, and I. A. Walmsley, Phys. Rev. A **62,** 013814 (2000).

[17] P. G. Kwiat, E. Waks, A. G. White, I. Appelbaum, and P. H. Eberhard, Phys. Rev. A **60,** R773 (1999); Y. H. Kim, S. P. Kulik, and Y. Shih, Phys. Rev. A **62,** 011802 (2000).

[18] M. Atatüre, A. V. Sergienko, B. E. A. Saleh, and M. C. Teich, Phys. Rev. Lett. **86**, 4013 (2001).

[19] A. G. White, D. F. V. James, W. J. Munro, and P. G. Kwiat, Phys. Rev. A **65**, 012301 (2002).

[20] N. Bloembergen, U.S. Patent 3,384,443, May 21, 1968; M. M. Fejer, G. A. Magel, D. H. Jundt, and R. L. Byer, IEEE J. Quant. Electron. **11**, 2631 (1992); P. Baldi, P. Aschieri, S. Nouh, M. De Micheli, D. B. Ostrowsky, D. Delacourt, and M. Papuchon, IEEE J. Quant. Electron. **31**, 997 (1995); M. A. Arbore, A. Galvanauskas, D. Harter,

M. H. Chao, and M. M. Fejer, Opt. Lett. **22**, 1341 (1997); G. Imeshev, A. Galvanauskas, D. Harter, M. A. Arbore, M. Proctor, and M. M. Fejer, Opt. Lett. **23**, 864 (1998); M. H. Chao, K. R. Parameswaran, M. M. Fejer, and I. Brener, Opt. Lett. **24**, 1157 (1999).

[21] S. Tanzilli, H. De Riedmatten, W. Tittel, H. Zbinden, P. Baldi, M. De Micheli, D. B. Ostrowsky, and N. Gisin, Electron. Lett. **37,** 26 (2001).

[22] M. H. Rubin, D. N. Klyshko, Y. H. Shih, and A. V. Sergienko, Phys. Rev. A **50,** 5122 (1994).

[23] M. H. Rubin, Phys. Rev. A **54,** 5349 (1996).

[24] D. R. Lide, Ed. *CRC Handbook of Chemistry and Physics*, 74th Ed. (CRC Press, Boca Raton, Fla., 1994), p. **10**-304.

FIGURES

FIG. 1. Control over the nonlinearity profile of the generation medium allows control over the SPDC state function $\Phi(\Delta)$. In the case of a monochromatic plane wave pump, $\Phi(\Delta)$ is simply the inverse Fourier transform of the nonlinearity profile $\chi^{(2)}(z)$. The upper figure shows a sketch of $|\Phi(\Delta)|^2$ for Type-II SPDC from a single bulk crystal of thickness L. The lower figure shows a sketch of $|\Phi(\Delta)|^2$ for SPDC from a crystal with sinusoidally varying nonlinearity. In principle, any weighting profile of the signal and idler photons can be obtained by a judicious choice of crystal structure.

FIG. 2. Impact of generation-medium symmetry on the weighting profile of SPDC pumped by a monochromatic plane wave. The upper figure shows $|\Phi(\Delta)|^2$ for SPDC from two bulk crystals of unequal thickness separated by dispersive linear medium. The lower figure shows $|\Phi(\Delta)|^2$ for SPDC generated by a cascade of two bulk crystals of equal thickness.

FIG. 3. Propagation of the signal and idler photons through arbitrary linear optical systems $\mathcal{H}_{\mathrm{A}_j}$ and $\mathcal{H}_{\mathrm{B}_j}$.

FIG. 4. Schematic of a polarization interferometer for which we compute quantum-interference patterns. In this illustration, collinear SPDC is generated in two bulk crystals of arbitrary thickness separated by an air gap.

FIG. 5. Sketch illustrating a heuristic approach to calculating quantum interference in the single-mode limit for two bulk crystals of the same material and thickness separated by a linear dielectric. The results are coincidence rates as shown in the bottom right inset. The coincidence-rate data in the upper left inset is from representative experiments. Details are provided in the text.

FIG. 6. A figure analogous to that of Fig. 5 for the case of two bulk crystals of unequal thickness.

FIG. 7. Visibility $|V(LD)|$ as a function of crystal separation d for the case of parallel optical axes. The curves are plots of Eq. (54) for aperture diameters $b = 2.5$ mm, 4.0 mm, and 5.0 mm. Solid, shaded, and open circles denote the maxima of visibility. The distance d_1 (see Fig. 4) is 750 mm. Note that the period of visibility modulation as a function of crystal separation d contracts for increasing aperture diameter.

FIG. 8. Visibility at $\tau = LD$ for two identical crystals in contact ($d = 0$) as a function of the $(1/e)$ width r of identical Gaussian apertures in each arm of the interferometer shown in Fig. 4. Solid (dotted) curves correspond to parallel (antiparallel) optical axes. Results for different crystal thicknesses L are shown concurrently. The curves were generated with the parameters $d_1 = 1$ m, $\lambda_{\rm p} = 2\pi/k_{\rm p} = 351.1$ nm and $|M| = 0.07$.

FIG. 9. Experimental apparatus used to study polarization interference in collinear SPDC from two cascaded crystals separated by an air gap of thickness d. Details are found in the text.

FIG. 10. Visibility function at the center of the interference region, $V(LD)$, as a function of crystal separation d. Symbols represent data from parallel (shaded circles) and antiparallel (open circles) optical axes. Note that in our experiments $V(LD) = 1$ corresponds to an interference dip, while $V(LD) = -1$ corresponds to an interference peak. Insets at top are representative interference patterns at extremes of $V(LD)$, taken with $d = 17.5$ mm and $d = 32.5$ mm. Solid curves are plots of Eqs. (54) and (60) for parallel and antiparallel orientations, respectively.

FIG. 11. Visibility function $V(LD)$ as a function of crystal separation d for three different aperture diameters in the case of parallel optical axes. Solid curves are plots of Eq. (54). Solid, shaded, and open circles are experimental data for aperture diameters $b = 2.5$ mm, 4.0 mm, and 5.0 mm, respectively. The distance d_1 (see Fig. 4) is 750 mm.

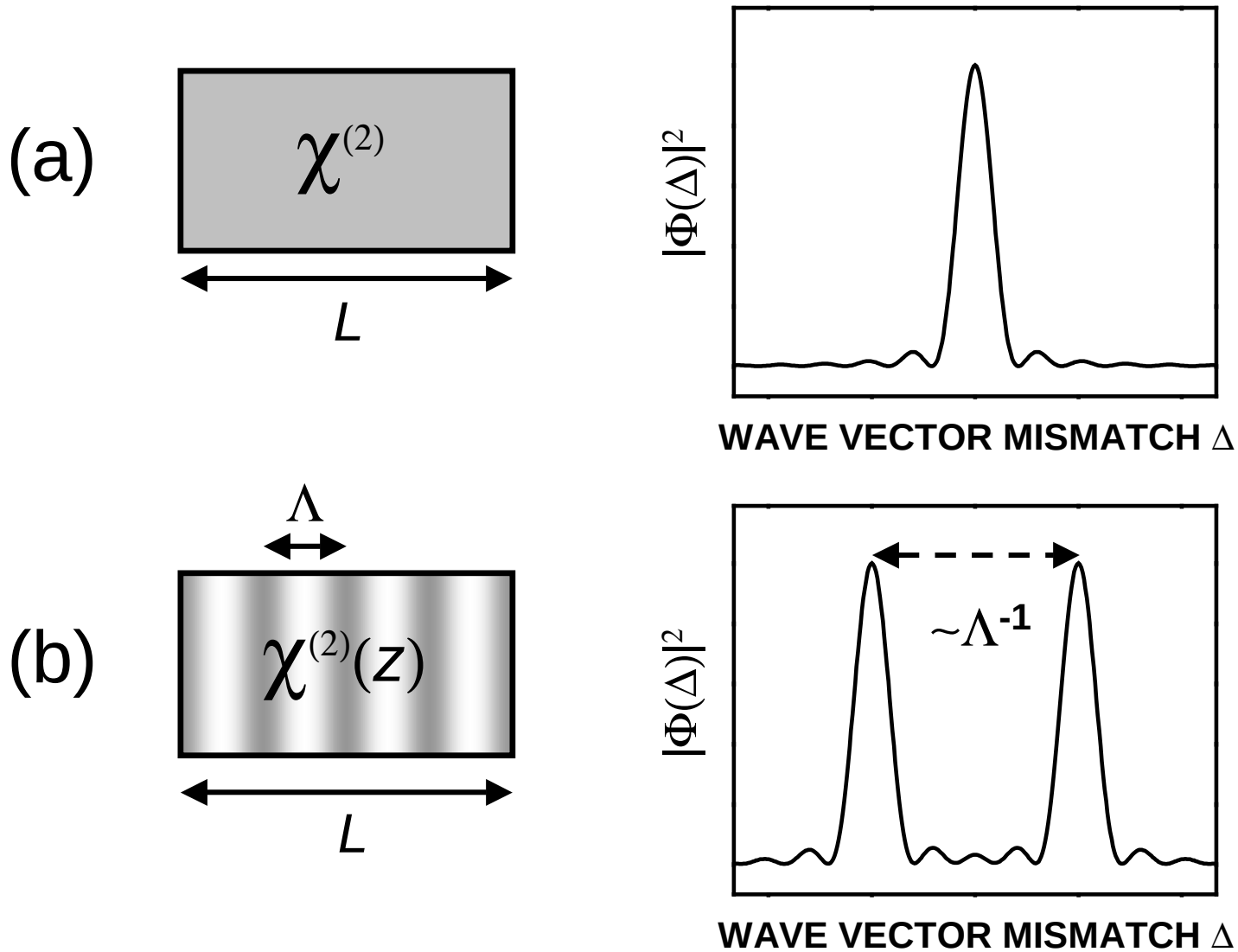
(a)
$\chi^{(2)}$
L
$|\Phi(\Delta)|^2$
WAVE VECTOR MISMATCH Δ
Λ
(b)
$\chi^{(2)}(z)$
L
$|\Phi(\Delta)|^2$
$\sim\Lambda^{-1}$
WAVE VECTOR MISMATCH Δ

Figure 1

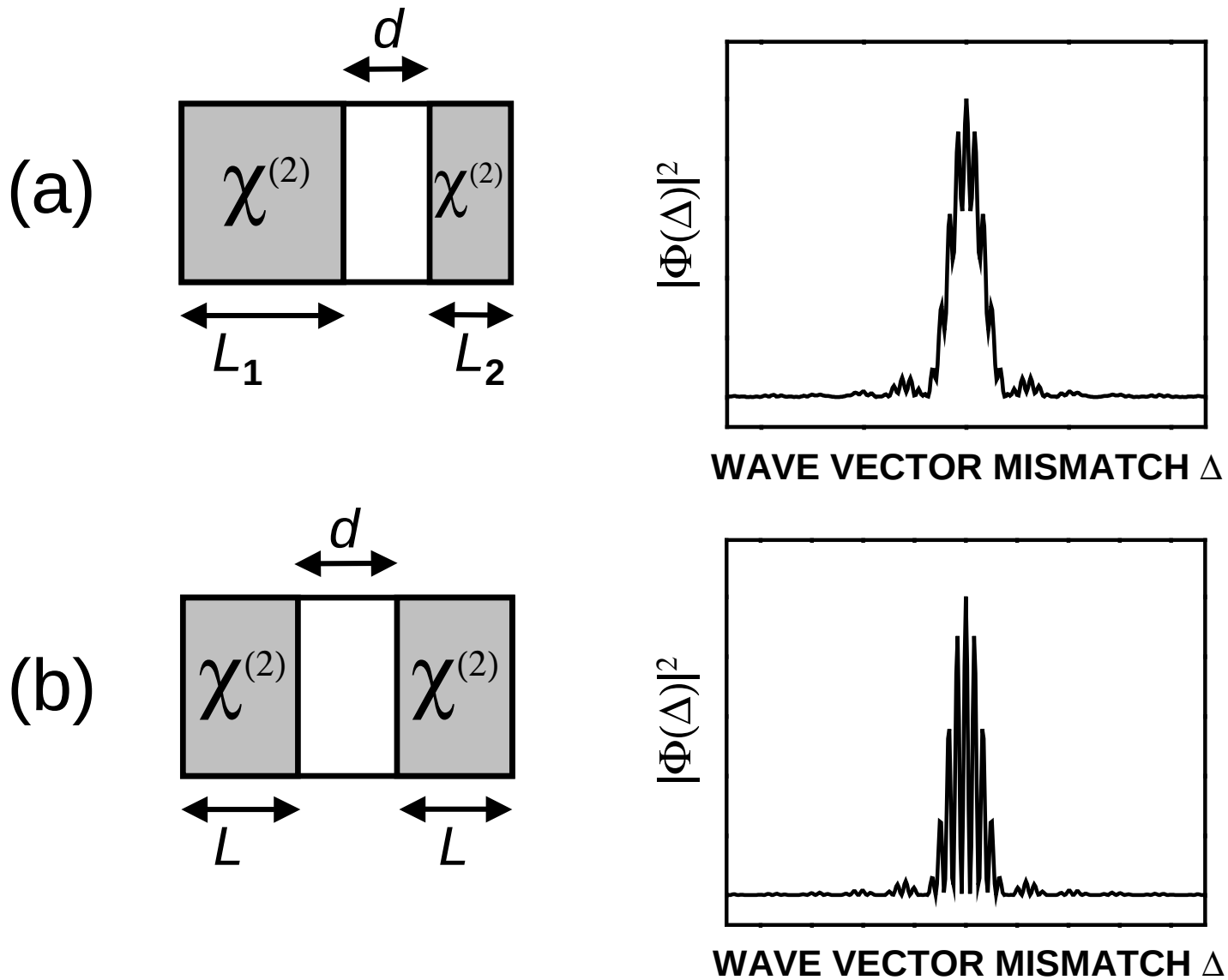
(a)
d
χ(2)
χ(2)
L1
L2
|Φ(Δ)|2
WAVE VECTOR MISMATCH Δ
(b)
d
χ(2)
χ(2)
L
L
|Φ(Δ)|2
WAVE VECTOR MISMATCH Δ

Figure 2

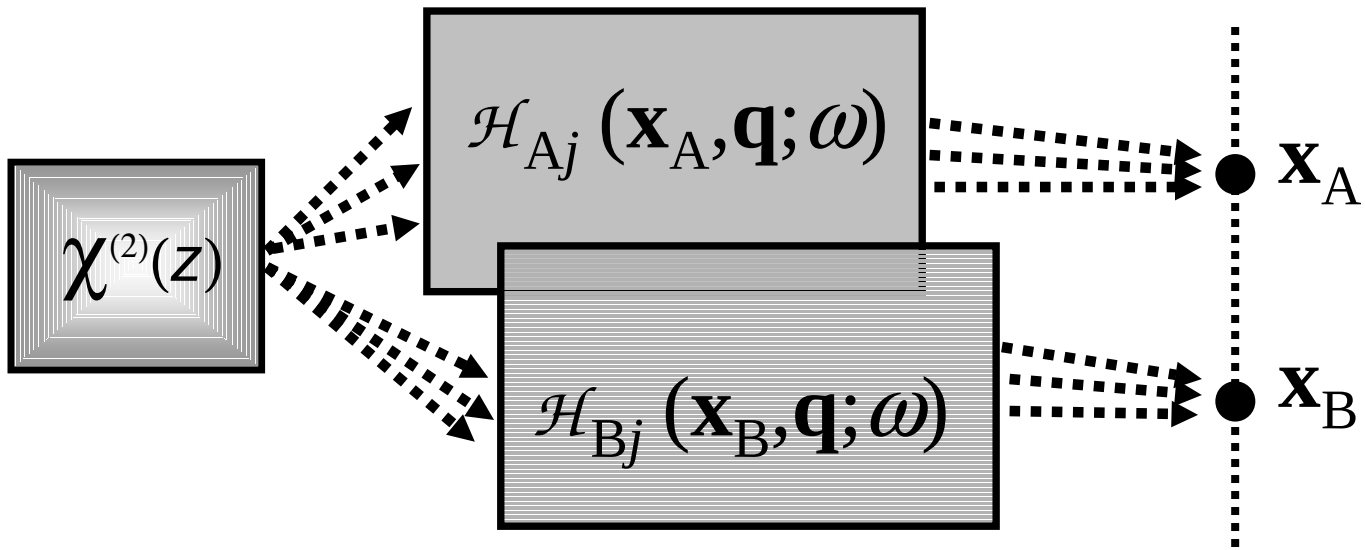
$\chi^{(2)}(z)$
$\mathcal{H}_{\mathrm{A}j}(\mathbf{x}_{\mathrm{A}},\mathbf{q};\omega)$
$\mathcal{H}_{\mathrm{B}j}(\mathbf{x}_{\mathrm{B}},\mathbf{q};\omega)$
$\mathbf{x}_{\mathrm{A}}$
$\mathbf{x}_{\mathrm{B}}$

Figure 3

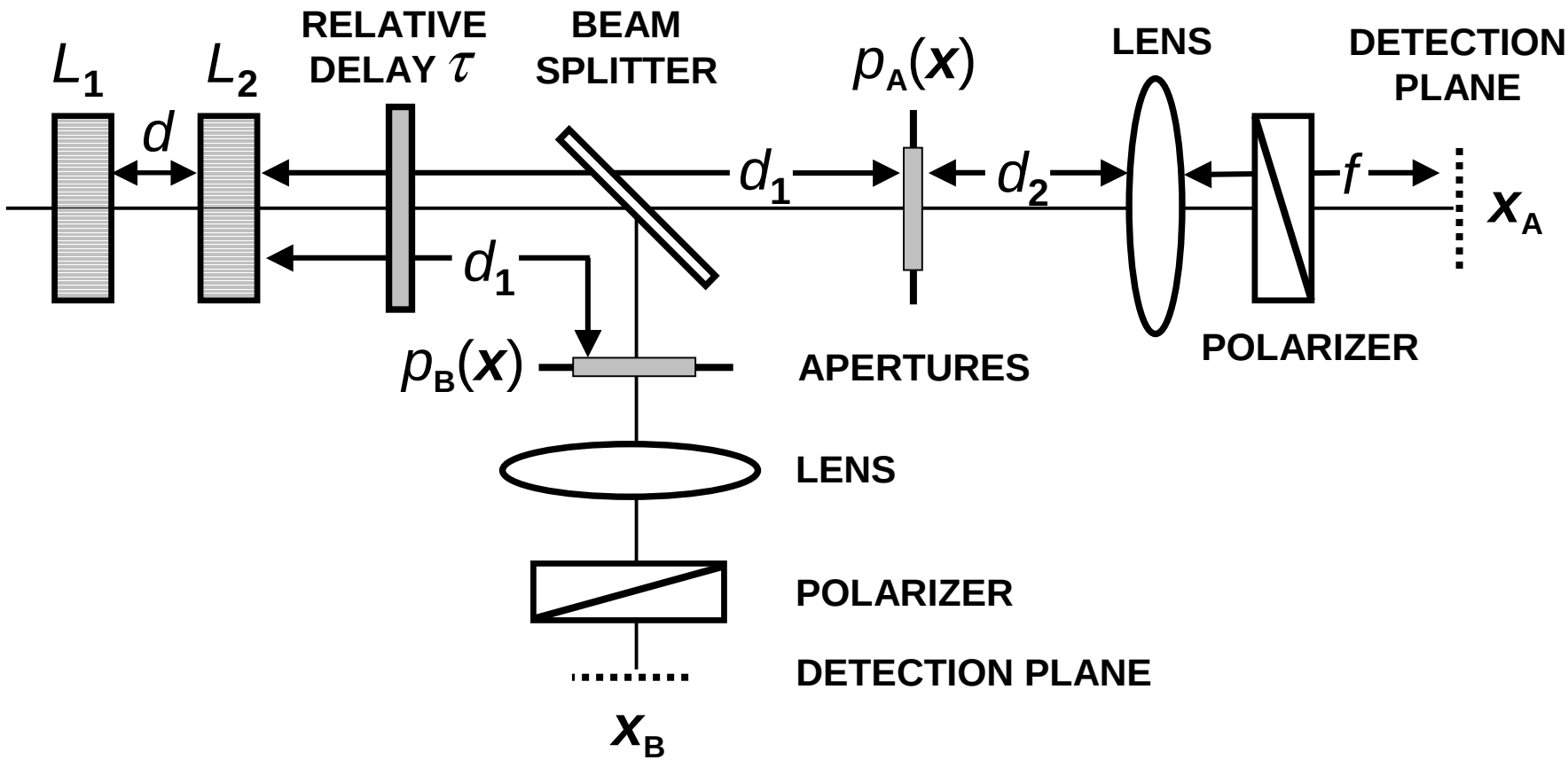
L_1
L_2
d
RELATIVE DELAY τ
BEAM SPLITTER
$p_A(x)$
LENS
DETECTION PLANE
d_1
d_2
f
x_A
d_1
$p_B(x)$
APERTURES
POLARIZER
LENS
POLARIZER
DETECTION PLANE
x_B

Figure 4

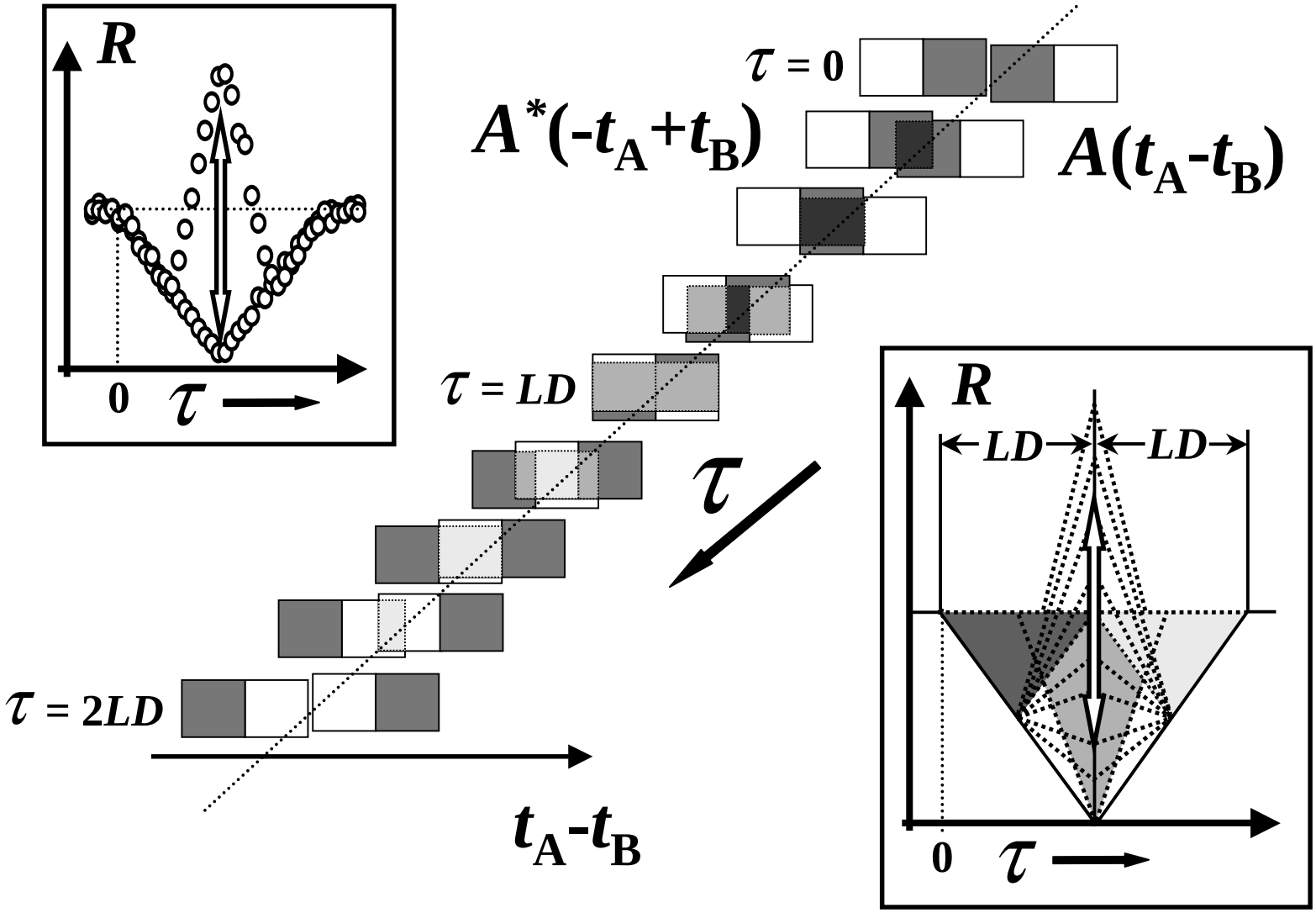

Figure 5

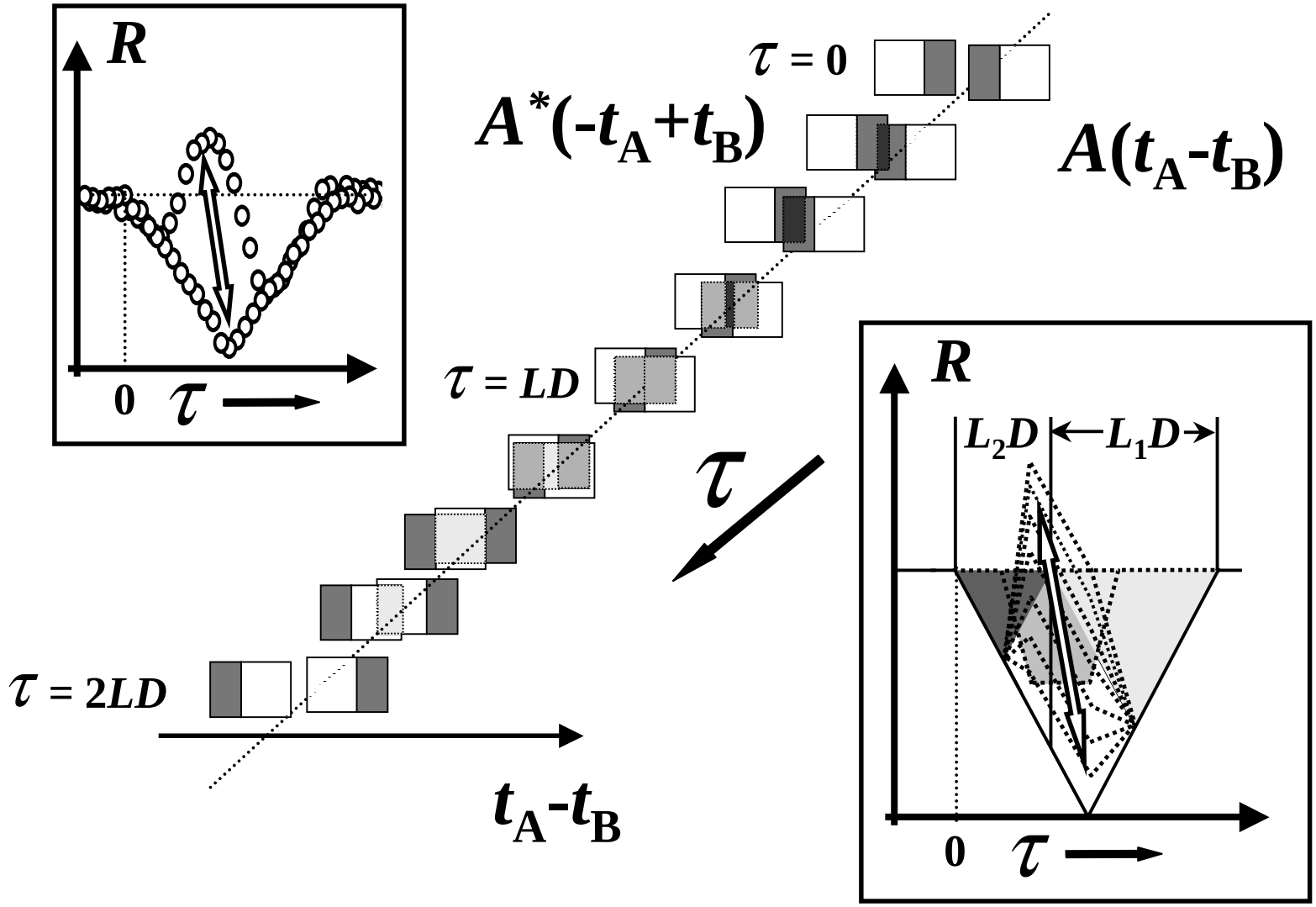

Figure 6

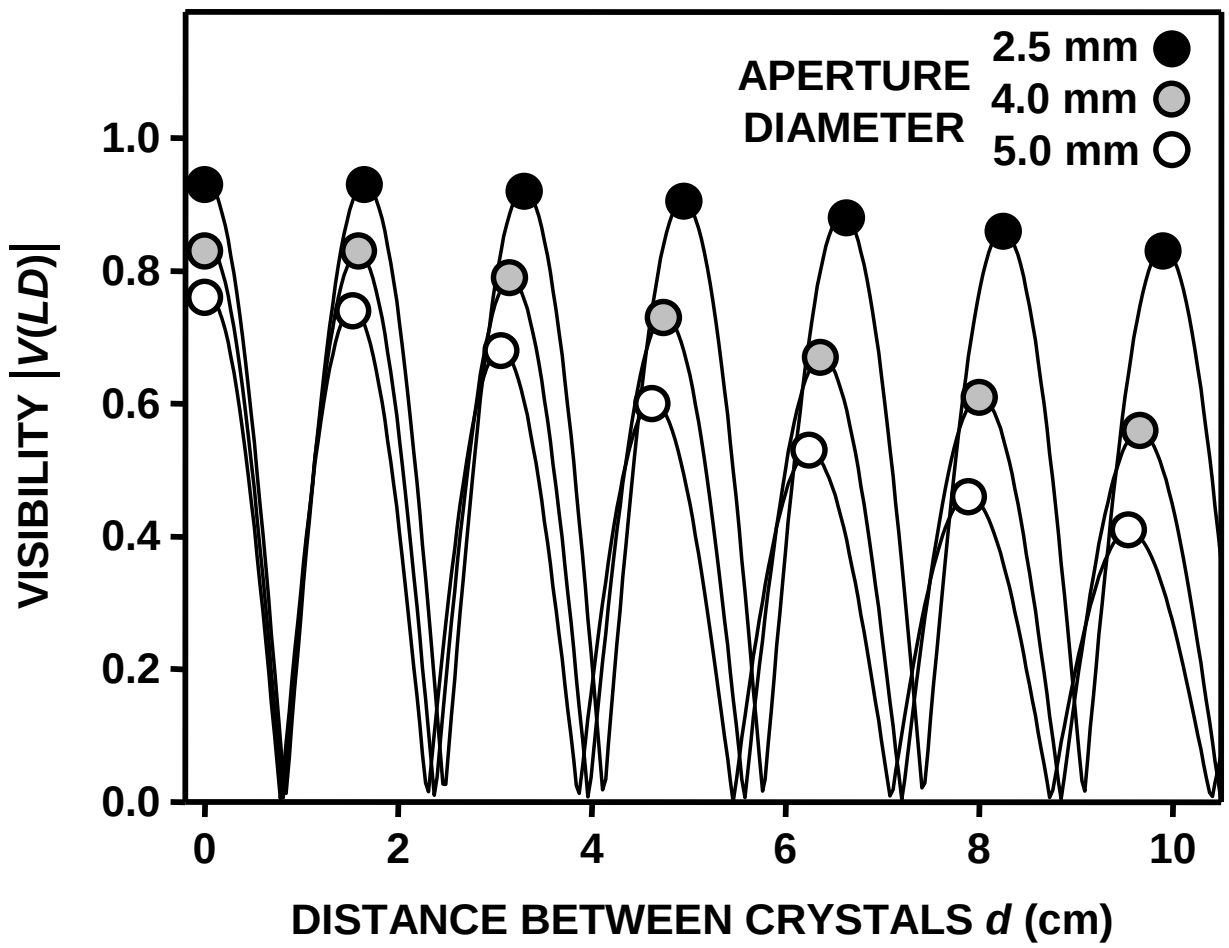
APERTURE DIAMETER
2.5 mm
4.0 mm
5.0 mm
VISIBILITY |V(LD)|
1.0
0.8
0.6
0.4
0.2
0.0
0
2
4
6
8
10
DISTANCE BETWEEN CRYSTALS d (cm)

Figure 7

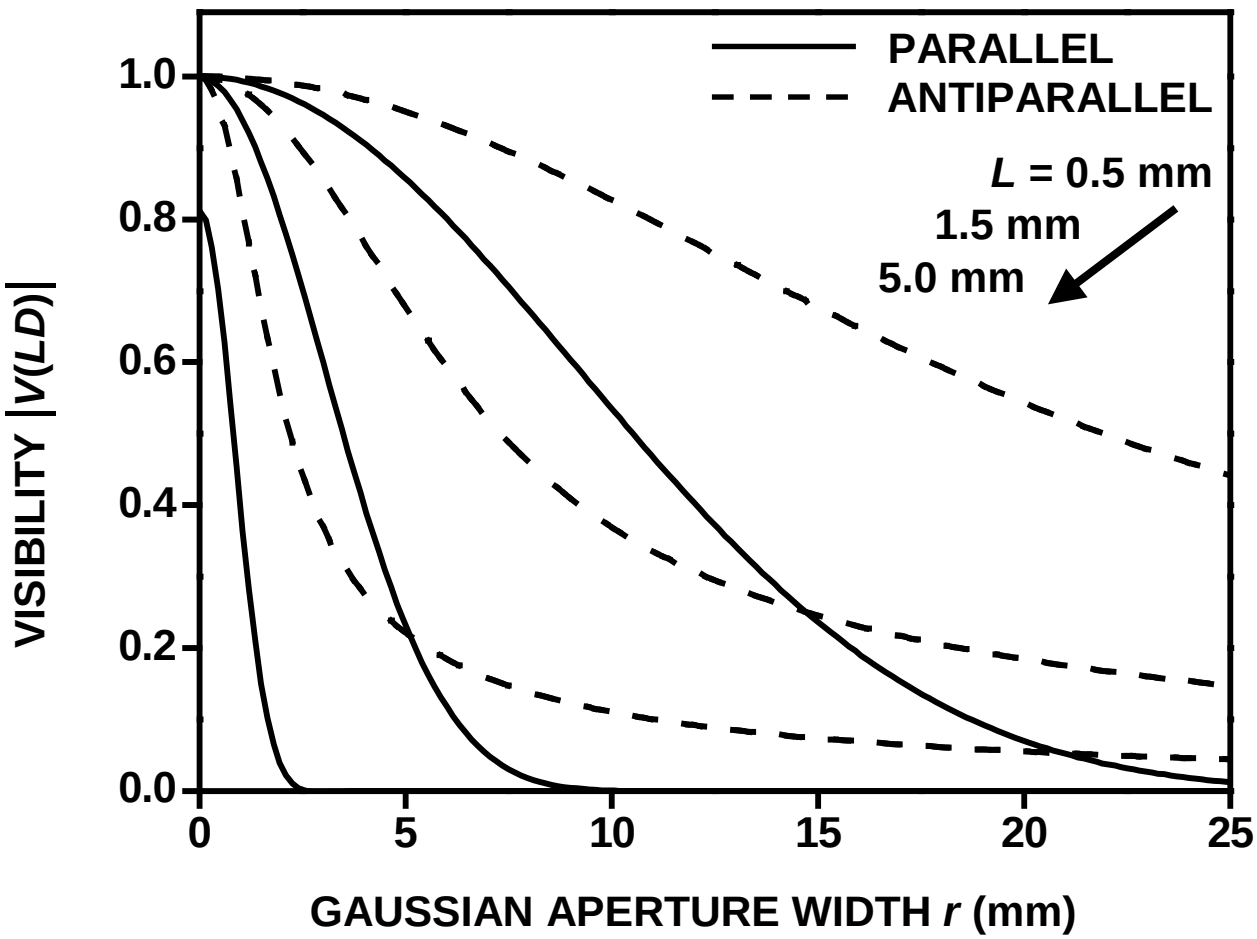
PARALLEL
ANTIPARALLEL
L = 0.5 mm
1.5 mm
5.0 mm
1.0
0.8
0.6
0.4
0.2
0.0
VISIBILITY |V(LD)|
0
5
10
15
20
25
GAUSSIAN APERTURE WIDTH r (mm)

Figure 8

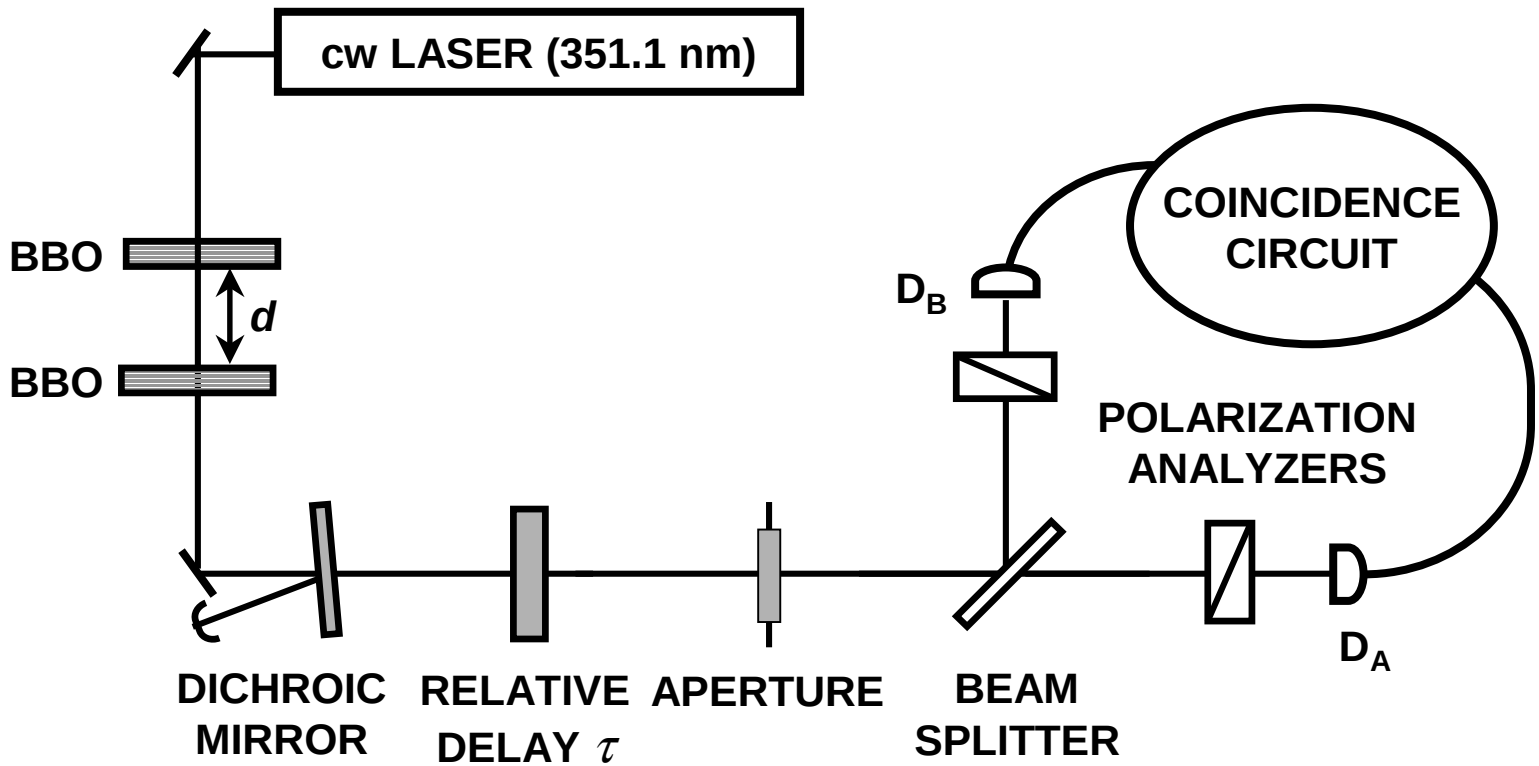
cw LASER (351.1 nm)
BBO
d
BBO
COINCIDENCE CIRCUIT
D_B
POLARIZATION ANALYZERS
D_A
DICHROIC MIRROR
RELATIVE DELAY τ
APERTURE
BEAM SPLITTER

Figure 9

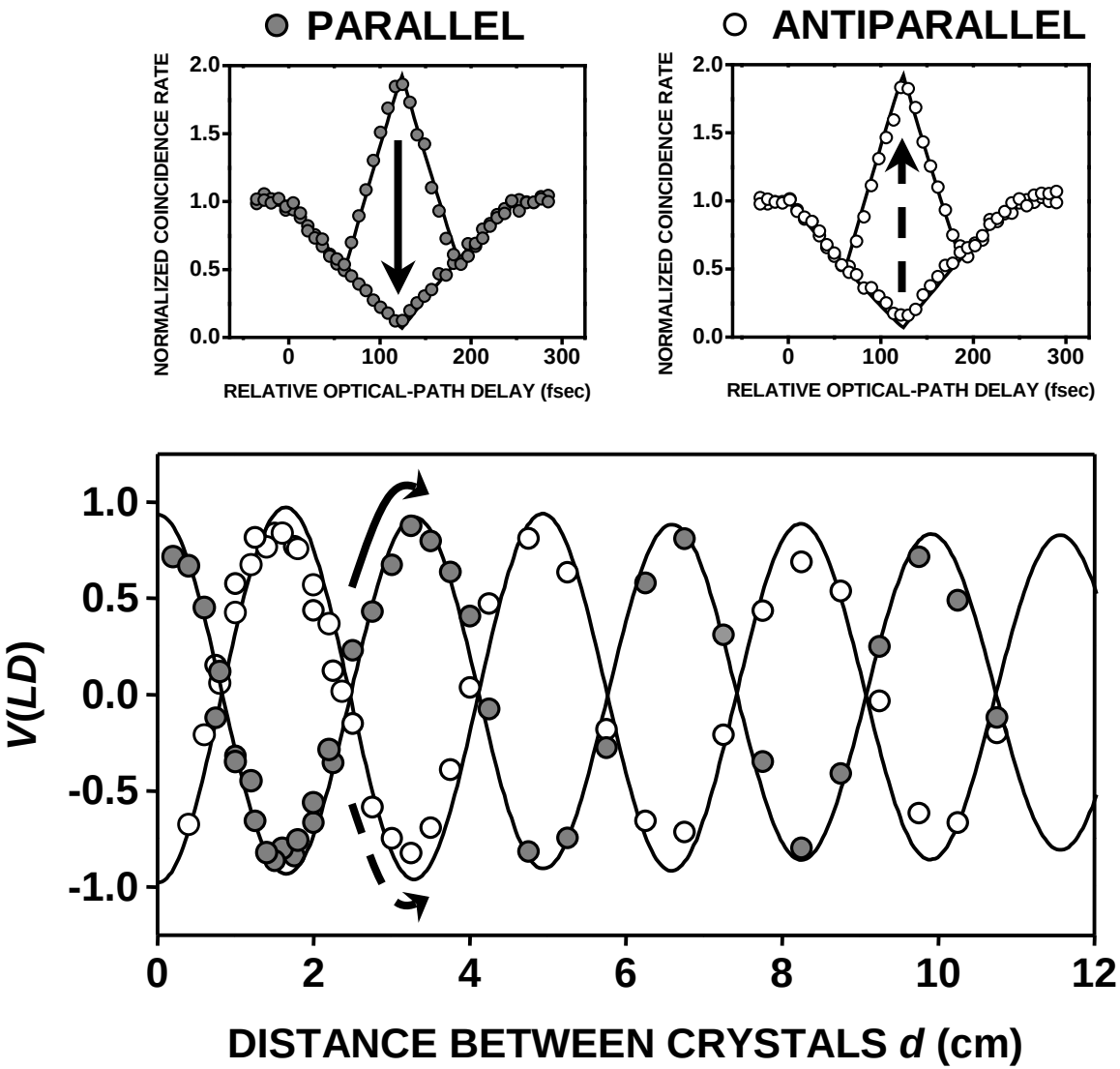
PARALLEL
ANTIPARALLEL
NORMALIZED COINCIDENCE RATE
2.0
1.5
1.0
0.5
0.0
0
100
200
300
RELATIVE OPTICAL-PATH DELAY (fsec)
V(LD)
1.0
0.5
0.0
-0.5
-1.0
0
2
4
6
8
10
12
DISTANCE BETWEEN CRYSTALS d (cm)

Figure 10

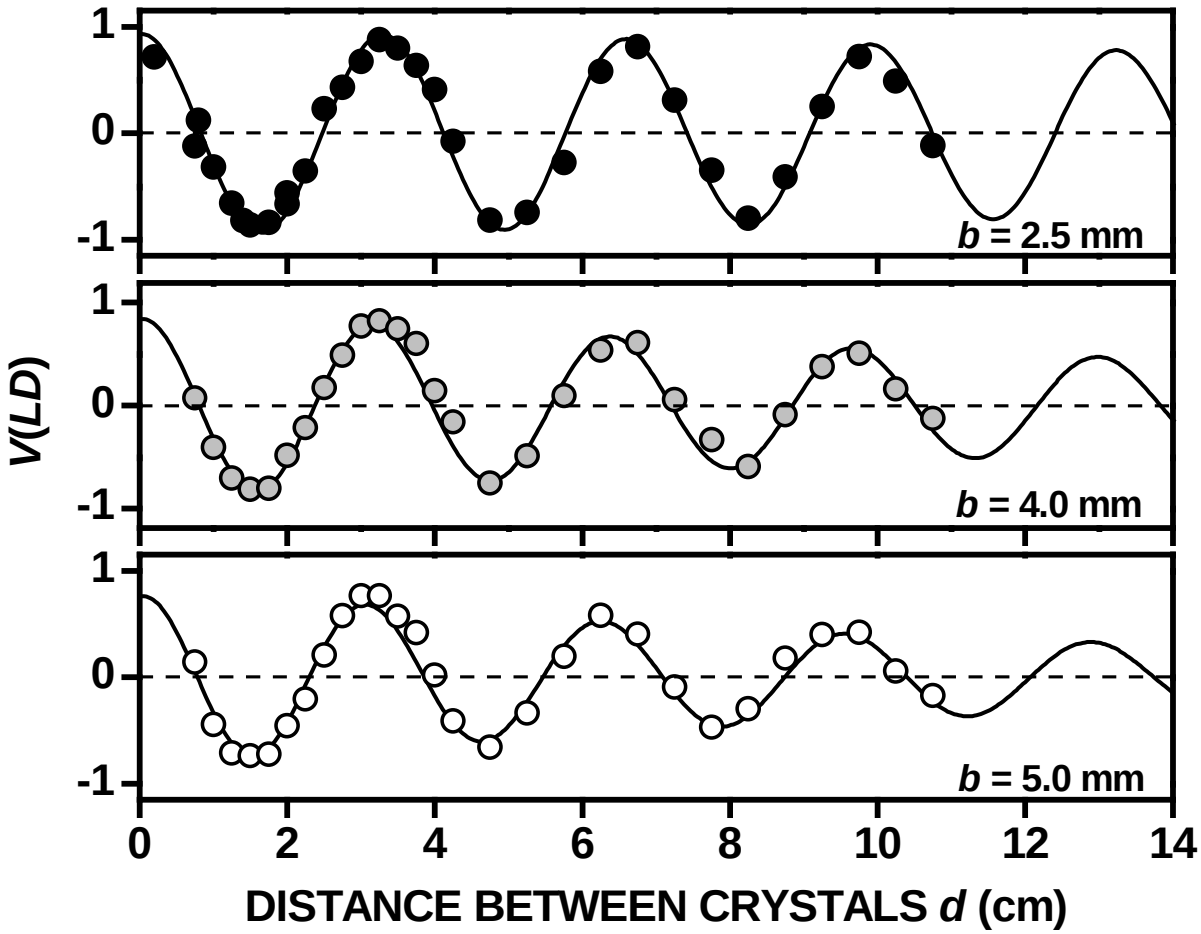
1
0
-1
b = 2.5 mm
b = 4.0 mm
b = 5.0 mm
V(LD)
0
2
4
6
8
10
12
14
DISTANCE BETWEEN CRYSTALS d (cm)

Figure 11